

Ab-initio insights into the mechanical, phonon, bonding, electronic, optical and thermal properties of hexagonal W₂N₃ for potential applications

Istiak Ahmed, F. Parvin, R. S. Islam, S. H. Naqib*

Department of Physics, University of Rajshahi, Rajshahi 6205, Bangladesh

*Corresponding author; Email: salehnaqib@yahoo.com

Abstract

We thoroughly investigated the structural, mechanical, electronic, vibrational, optical, thermodynamic and a number of thermophysical properties of W₂N₃ in this study through first-principles calculations utilizing the DFT based formalisms. The calculated lattice parameters show excellent agreement with the available theoretical and experimental results. The mechanical and dynamical stabilities of this compound have been confirmed theoretically from the calculated elastic constants and phonon dispersion curves of W₂N₃. The Pugh's and Poisson's ratios of W₂N₃ are located quite close to the brittle/ductile borderline. W₂N₃ is elastically anisotropic. The calculated electronic band structure and density of states reveal that W₂N₃ is metallic in nature. The Fermi surface topology has also been explored. The analysis of charge density distribution map clearly shows that W atoms have comparatively high electron density around than the N atoms. Presence of covalent bondings between W-N, W-W, and N-N atoms are anticipated. High melting temperature and high phonon thermal conductivity at room temperature of W₂N₃ imply that the compound has potential to be used as a heat sink system. The optical characteristics demonstrate anisotropy for W₂N₃. The compound can be used in optoelectronic device applications due to its high absorption coefficient and low reflectivity in the visible to ultraviolet spectrum. Furthermore, the quasi-harmonic Debye model is used to examine temperature and pressure dependent thermal characteristics of W₂N₃ for the first time.

Keywords: Tungsten nitride; Density functional theory; Mechanical properties; Phonon dynamics; Thermal properties; Optoelectronic properties

1. Introduction

Due to the importance in both fundamental science and technological applications, the investigation of superhard materials has always been an interesting topic [1-3]. Researchers

have synthesized two groups of superhard materials; one of them is formed by the light elements (e.g. B, C, N, O etc.) such as diamond, cubic boron nitride and carbon nitrides [4-7], the other group comprises the borides, carbides, nitrides and oxides of transition metals (TMs) [8-10]. Recently, there has been a lot of interest in transition metal nitrides due to their distinctive mechanical, electronic, catalytic, optical, and magnetic characteristics for technological applications as well as their basic significance in condensed matter physics [11-19]. Various transition metal nitrides and their allotropes have also been reported and have attracted significant attention due to their unique physical and mechanical properties including high catalytic activity, chemical inertness, extreme hardness etc. [20-24].

Due to the extended lives and increased wear resistance that higher hardness offers, industries frequently seek superhard materials for tools utilized in heavy duty operations. These materials often need high-pressure, high-temperature (HPHT) conditions to form, thus, conventional ultra-hard materials like diamond and cubic boron nitride (*c*-BN) are expensive and challenging to make. Due to these restrictions, research has been concentrated on finding innovative superhard materials that are less expensive to manufacture. Compounds containing the light elements C, B, O, and N are shown to be effective candidates. The next generation of superhard materials is being paved by the transition metal borides, which among these contenders have great hardness and are easily produced under ambient circumstances [25]. It has been demonstrated through experiments that the N-to-W ratio in the WN compounds may vary, which correlates to various W_xN_y crystals. As a result, the synthesized WN compounds have very complex structures. Early measurements showed the structures of a number of WN compounds, including hexagonal WN, [26] hexagonal and rhombohedral W_2N_3 , cubic W_3N_4 , [23] NaCl type WN [27]. Recently, Balasubramanian *et al.* [28] used the first-principles technique to explore the stability of WN compounds and discovered that whereas WN is mechanically unstable in cubic structures, it is mechanically stable in the NbO structure. It is important to note that because tungsten nitride exists in a number of phases with a wide range of compositions, it is likely that certain stable WN crystal forms were not visible in earlier investigations. The WN_6 is a structure that has just been predicted, and it is thermodynamically stable at high pressure [20]. Recently, first-principles simulations by Mounet *et al.* [29] demonstrate that two-dimensional W_2N_3 may easily exfoliate from a layered hexagonal bulk W_2N_3 ; the latter was first observed experimentally by Wang *et al.* in 2012 [23]. W_2N_3 is an excellent candidate for mechanical exfoliation because its binding energy is 26.3 meV, which is very similar to the values

calculated for the most prevalent transition-metal dichalcogenides [23]. David Campi *et al.* [30] found intrinsic superconductivity in monolayer W_2N_3 with a critical temperature of 21 K, just above that of liquid hydrogen by means of first-principles calculations. Jing-Yang You *et al.* [31] reported a detailed investigation of the superconductivity and non-trivial electronic topology in 2D monolayer W_2N_3 . They found that monolayer W_2N_3 is a superconductor with transition temperature of about 22 K and has a superconducting gap of 5 meV, based on the anisotropic Migdal-Eliashberg formalism.

To the best of our knowledge, only a few of the physical properties of bulk W_2N_3 have been studied so far, including its structural properties, bulk modulus and its pressure derivative, electronic properties (band structure, density of states and Fermi surface), phonon spectra and superconducting transition temperature [30, 32]. There are still many unexplored significant physical aspects of W_2N_3 . Remarkably, most of the physical characteristics relevant to prospective applications, e.g., electronic charge density distribution, various mechanical properties, Mulliken bond population analysis, theoretical hardness, optical properties, thermodynamic properties of W_2N_3 have not been explored at all till date. The aim of this study is to look at these unexplored physical properties in detail. Some of the physical properties have been revisited for validation and completeness. The results presented herein shows that W_2N_3 is a highly promising compound for applications in the engineering and optoelectronic device sectors.

The remaining parts of this manuscript are structured as follows: In Section 2, an in-depth description of the computational methodology used in the present study can be found. In Section 3, an extensive discussion of the investigated properties and their possible consequences was presented. In Section 4, the important features from our study are summarized and discussed.

2. Computational methodology

The main DFT tool used in this investigation was the CASTEP code [33]. The potential for electronic exchange correlation was assessed using the Perdew–Burke–Ernzerhof scheme for solids (PBEsol) functional within the generalized gradient approximation (GGA) [34]. The Vanderbilt-type ultra-soft pseudopotential [35] was used to simulate the interactions between electrons and the ion cores. The basis sets for the valence electron states for W and N were $5s^25p^65d^46s^2$ and $2s^22p^3$, respectively. The first Brillouin zone in the reciprocal space of the

hexagonal unit cell of W_2N_3 is integrated over using the Monkhorst-Pack (MP) technique [36] with a k-point mesh of $26 \times 26 \times 5$ grid. The eigenfunctions of the valence and nearly valence electrons were expanded using a plane-wave basis at a cutoff energy of 550 eV. Using the Broyden-Fletcher-Goldfarb-Shanno (BFGS) technique [37], the internal forces and total energy were both relaxed during the geometry optimization. The highest ionic Hellmann-Feynman force was less than 0.03 eV/\AA , the maximum ionic displacement was less than $1 \times 10^{-3} \text{ \AA}$, the maximum stress was less than 0.05 GPa and the tolerance for total energy was less than 10^{-5} eV/atom in order to accomplish the self-consistent convergence.

The DFT-based finite strain method [38] is used to determine the elastic characteristics. This approach relaxes the atomic degrees of freedom by applying a series of finite uniform deformations on the typical unit cell. The single crystal elastic constants C_{ij} are then determined from the resulting stresses using a series of linear expressions:

$$\sigma_{ij} = \sum_{ij} C_{ij} \delta_{ij} \quad (1)$$

where δ_{ij} stands for the six stress components that are applied to each strain on the conventional unit cell. The bulk and shear elastic moduli of polycrystalline materials, which are determined using this method, are calculated using the well-known Voigt-Reuss-Hill approximations [39–41]. The maximum force within 0.006 eV/\AA and the maximum ionic displacement within $2 \times 10^{-4} \text{ \AA}$ are fixed as the convergence condition for estimating the elastic characteristics.

The calculation of electronic charge density distribution and Fermi surface requires that k-point spacing has to be less than 0.01 \AA^{-1} . So, we have chosen a k-point mesh of $40 \times 40 \times 7$ grids in this work. Using the density functional perturbation theory (DFPT) based finite-displacement method (FDM) [42-43], which is embedded into the CASTEP code, the dynamical stability and lattice dynamic properties such as phonon dispersion and phonon density of states were calculated.

From the complex dielectric function $\varepsilon(\omega) = \varepsilon_1(\omega) + i\varepsilon_2(\omega)$, the frequency dependent optical constants of W_2N_3 have been derived. The momentum matrix elements between the unoccupied and the occupied electronic orbitals can be used to obtain the imaginary part of the dielectric function, $\varepsilon_2(\omega)$ by using the following equation:

$$\varepsilon_2(\omega) = \frac{2\pi e^2}{\Omega \varepsilon_0} \sum_{k,v,c} |\psi_k^c| \mathbf{u} \cdot \mathbf{r} |\psi_k^v|^2 \delta(E_k^c - E_k^v - E). \quad (2)$$

where, Ω is the unit cell volume, ω is the angular frequency of the incident phonon, e is the charge of an electron, ψ_k^c and ψ_k^v are respective wave functions for conduction band and valence band electrons at a specific k , and \mathbf{u} is the unit vector defining the polarization direction of the incident electric field. Using the Kramers-Kronig transformation equation, the real part of the dielectric function, $\varepsilon_1(\omega)$, has been determined from the corresponding imaginary part, $\varepsilon_2(\omega)$. The other optical functions, namely, the absorption coefficient $\alpha(\omega)$, reflectivity $R(\omega)$, refractive index $n(\omega)$, energy loss-function $L(\omega)$, and optical conductivity $\sigma(\omega)$, can be deduced from the estimated values of $\varepsilon_1(\omega)$ and $\varepsilon_2(\omega)$ using the expressions found in the literature [44].

The quasi-harmonic Debye model, as implemented in the Gibbs program [45], is used to investigate the thermodynamic properties at different temperatures and pressures. We have utilized the E - V data and used the third-order Birch-Murnaghan equation of state (EOS) [46, 47] and equilibrium values of E_0 , V_0 , and B_0 obtained using the DFT method at zero temperature and zero pressure for finite temperature/pressure computations.

3. Results and discussion

3.1 Structural optimization and phase stability of W_2N_3

The optimized crystal structure of W_2N_3 is depicted in Fig. 1. W_2N_3 crystallizes in hexagonal structure with space group $P6_3/mmc$ (No. 194) [23] and has a layered structure. There are two formula units and ten atoms per unit cell. Fully relaxed structure for W_2N_3 is obtained by optimizing the geometry including the lattice constants and internal atomic positions. The optimized W atom is located at the $4f$ Wyckoff position, with fractional coordinates (1/3, 2/3, 0.840), and N atom is located at the $4f$ and $2c$ Wyckoff positions, with fractional coordinate (1/3, 2/3, 0.070) and (1/3, 2/3, 1/4), respectively [23]. Table 1 represents the values of lattice constants a and c , equilibrium unit cell volume V , internal atomic coordinate z , and the formation enthalpy ΔH for W_2N_3 at ambient pressure. The lattice parameter of W_2N_3 was first reported in 2012 with $a = 2.890 \text{ \AA}$ and $c = 15.286 \text{ \AA}$ [23]. Y. Wang *et al.* reported the lattice parameters of W_2N_3 for the second time with $a = 2.870 \text{ \AA}$ and $c = 15.175 \text{ \AA}$ [48]. The optimized lattice parameters of our study are found to be 2.888 \AA and 15.807 \AA for a and c , respectively. These values are highly consistent with those found in previous studies. The

negative value of enthalpy reveals that, at ambient pressure, tungsten nitride in the hexagonal structure is thermodynamically stable.

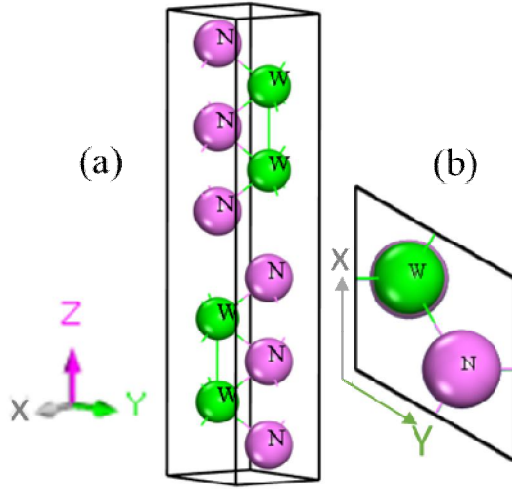


Fig. 1. (a) Conventional unit cell of W_2N_3 and (b) its 2D view in the xy -plane

Table 1. Calculated and previously obtained experimental/theoretical lattice constants (a , b , and c) (all in \AA), unit cell volume (V in \AA^3), internal coordinate (z), and enthalpy of formation (ΔH in eV/atom) of W_2N_3 .

a	b	c	V	z	ΔH	Ref.
2.888	2.888	15.807	114.14	0.088	-2.23	This work
2.890	2.890	15.286	--	---	---	[23] ^{expt.}
2.870	2.870	15.175	108.22	---	---	[48] ^{theo.}

3.2 Mechanical properties

Elastic constants are very important material characteristics. The elastic constants of crystalline solids provide the link between mechanical and dynamical behavior of crystal under external stress of different types concerning the nature of the forces operating in solids, especially for the stability and stiffness of materials. The elastic constants are correlated with a material's mechanical characteristics, including stability, stiffness, brittleness, ductility, and elastic anisotropy. For engineering purposes, these characteristics are crucial when choosing a material for a specific task. According to the Born-Huang conditions, a hexagonal system has to satisfy the following inequality requirements in order to be mechanically stable [49]:

$$C_{11} - |C_{12}| > 0,$$

$$(C_{11} + C_{12})C_{33} - 2C_{13}^2 > 0,$$

$$C_{44} > 0$$

W_2N_3 has positive values for each of its elastic constants C_{ij} as shown in Table 2 and satisfies the above stability requirements, indicating that it is mechanically stable.

Table 2. Calculated elastic constants, (C_{ij} in GPa), tetragonal shear modulus, (C' in GPa) and the internal strain parameter (ξ) of W_2N_3 .

Compound	C_{11}	C_{12}	C_{13}	C_{33}	C_{44}	C_{66}	C'	ξ	Ref.
W_2N_3	535.1	204.0	7.7	38.8	11.8	165.5	165.5	0.522	This work
	570	205.0	14.0	85.0	30.0	--	--	--	[48] ^{theo.}

Every elastic constant has a different meaning; for example, the resistance to linear compressions in the [100] and [001] directions can be measured by the elastic constants C_{11} and C_{33} , respectively. The bonding strength in W_2N_3 is stronger and compressibility is lesser along [100] direction than along [001] direction as C_{11} is much greater than C_{33} . Elastic constant C_{44} stands for the compound's resistance to shear deformation with respect to a tangential stress applied to the (100) plane in the [010] direction. According to our computed values, C_{44} is substantially lower than C_{11} and C_{33} . According to this W_2N_3 deforms more readily under shear than under unidirectional stress. The off-diagonal shear components are represented by the elastic constants C_{12} and C_{13} , which are connected to the resistance of a compound as a result of shears in different crystal planes. The resistance of the (100) plane to shear in the [110] direction is correlated with the elastic constant C_{66} . C_{44} has a somewhat lower value for the compound under study than C_{66} . For W_2N_3 , $(C_{11} + C_{12}) > C_{33}$, which predicts that the elastic tensile modulus, is greater in the (001) plane than it is along the c -axis and thus the bonding in the (001) plane is elastically stiffer than that along the c -axis. Another measure of crystal's stiffness, known as the tetragonal shear modulus, is determined by the following equation:

$$C' = \frac{(C_{11} - C_{12})}{2} \quad (3)$$

This parameter indicates the dynamic stability of a material. If C' is greater than zero, the compound is stable; otherwise, it is dynamically unstable. In Table 2, the tetragonal shear modulus for W_2N_3 is reported to be 165.5 GPa (positive), thus W_2N_3 is predicted to be dynamically stable. A dimensionless internal strain parameter, known as the Kleinman parameter (ξ), is a measure of stability of a compound against stretching and bending. To compute this parameter for W_2N_3 , the following equation has been used [50]:

$$\xi = \frac{(C_{11} + 8C_{12})}{(7C_{11} + 2C_{12})} \quad (4)$$

ξ has the value in the range $0 \leq \xi \leq 1$. The upper and lower limits of ξ are respectively represented by the significant contribution of bond bending to resist the external stress and the significant contribution of bond stretching to resist the external stress. The estimated values of ξ of W_2N_3 is 0.522, from which it can be predicted that mechanical strength in W_2N_3 is almost equally affected by bond bending and bond stretching/contracting. Additionally, the Kleinman parameter describes how the cation and anion sub-lattices' relative position shifts in the crystal when volume-conserving distortions cause atomic locations to alter in ways not ensured by the ground state crystal symmetry.

While the elastic moduli produced via the Voigt-Reuss-Hill (VRH) approximation are often based on polycrystalline aggregates of compounds, the elastic constants estimated from DFT are based on single crystals. The following relationships [51-53] are used to estimate the Hill approximations [41] for the bulk modulus (B_H), shear modulus (G_H), Young's modulus (Y), Poisson's ratio (ν), and hardness (H) of W_2N_3 :

$$B_H = \frac{(B_V + B_R)}{2} \quad (5)$$

$$G_H = \frac{(G_V + G_R)}{2} \quad (6)$$

$$Y = \frac{9BG}{(3B + G)} \quad (7)$$

$$\nu = \frac{(3B - 2G)}{2(3B + G)} \quad (8)$$

$$H = \frac{(1 - 2\nu)}{6(1 + \nu)} \quad (9)$$

The elastic moduli (bulk modulus B , shear modulus G , and Young's modulus Y) characterize how the materials in the polycrystalline aggregates behave mechanically under loading. The resulting values are given in Table 3. The bulk modulus, B , shows resistance to fracture, whereas the shear modulus G , represents resistance to plastic deformation. For W_2N_3 , a lower

value of G relative to B as shown in Table 3 indicates that the mechanical strength will be constrained by plastic deformation. The bulk modulus (B) is inversely proportional to the cell volume (V) [54]. As a result, the bulk modulus B , which has a significant association with the cohesive energy or binding energy of the atoms in crystals, might be employed as a measure of the average atomic bond strength of materials [55]. On the other side, a high shear modulus value indicates that strong directional bondings are present between atoms [56]. Young's modulus can be used to calculate the resistance of a material to tension or compression along its length. The critical thermal shock coefficient is inversely proportional to the Young's modulus Y [57], which means that the Young's modulus has an impact on a material's ability to resist thermal shock. Better thermal shock resistance is associated with higher R values. For the selection of thermal barrier coating (TBC) materials, the thermal shock resistance is a crucial factor. The high value of Y as shown in Table 3 indicates that W_2N_3 is capable of high resistance to thermal shock. In general, larger values of Young's modulus suggest higher stiffness for a particular class of materials [58]. The calculated Young's modulus of our studied compound is quite medium; therefore, it is a moderately stiff material. Various thermophysical parameters and elastic moduli are interrelated. For example, a material's lattice thermal conductivity (k_1) and Young's modulus (Y) are connected as $k_1 \sim \sqrt{Y}$ [59].

The factors, such as the Pugh's ratio (G/B) and the Poisson's ratio (σ) can characterize materials brittle or ductile nature [60-62]. The shear modulus to bulk modulus ratio (G/B) was suggested by Pugh [61] in 1954 as a useful measure for determining the brittleness and ductility of materials. 0.57 is the key value that distinguishes brittle from ductile materials. A value higher than 0.57 is associated with brittleness, whereas a value lower than 0.57 is correlated with ductility. Frantsevich *et al.* [62] also distinguished between brittleness and ductility in terms of the Poisson's ratio, and they proposed that 0.26 act as the boundary between brittle and ductile nature. The material will be brittle if the Poisson's ratio is less than 0.26; or else, the material will be ductile. The Pugh's ratio (G/B) and Poisson's ratio of W_2N_3 is 0.577 and 0.258, respectively. These values indicate that the mechanical state of W_2N_3 is located quite close to the brittle/ductile borderline.

The lower and upper limits of Poisson's ratio for a solid for central-forces are 0.25 and 0.50, respectively [63, 64]. We can predict from the values of Poisson's ratio as shown in Table 3 that the interatomic force of W_2N_3 is central in nature. The Poisson's ratio can be employed

as well to identify if a material has covalent or ionic bonds. The values of σ for ionic and covalent materials are generally 0.25 and 0.10, respectively [65]. Our computed Poisson's ratio of W_2N_3 is 0.258 suggesting that W_2N_3 contains ionic contribution.

The term *machinability* refers to the characteristic of a material that determines how easily it may be machined using a cutting tool. In engineering manufacturing and production, this parameter is used frequently. The work material, cutting tool, and cutting settings are a few of the variables that affect machinability. The choice of cutting tool material, tool shape, cutting force, feed rate, and depth of cut are all determined by the machinability of a given material. Furthermore, it determines the solid's dry lubricating properties and plasticity [66-69]. The formula for calculating a material's machinability index, μ_M , is [70]:

$$\mu_M = \frac{B}{C_{44}} \quad (10)$$

A compound with a low C_{44} value provides superior dry lubricity, according to this equation. A compound with a higher B/C_{44} value has better lubricating qualities, lower feed forces, lower friction, and greater plastic strain values. W_2N_3 has a B/C_{44} value of 8.62. This implies a very high level of machinability.

For the purpose of ensuring product quality in industry, the study of material hardness is of utmost importance. It illustrates how a material is affected by high loads. To understand elastic and plastic properties of a compound, measurement of hardness is crucial. The hardness of solid materials can be expressed into two broad categories. These are (i) soft material whose hardness is less than 10 GPa and (ii) hard material whose hardness is higher than 10 GPa [71-73]. W_2N_3 has estimated hardness of 9.69 GPa, which is reported in Table 3. This value indicates that W_2N_3 is moderately hard.

Table 3. The calculated bulk modulus (B in GPa), shear modulus (G in GPa), Young's modulus (Y in GPa), Pugh's indicator (G/B), machinability index (μ_M), Poisson's ratio (σ) and Vickers hardness (H_V in GPa) of W_2N_3 .

Compound	B	G	Y	G/B	σ	μ_M	H_V	Ref.
W_2N_3	104.15	60.10	151.21	0.577	0.258	8.62	9.69	This work
	131.00	84.00	--	0.640	--	--	13.00	[48] ^{theo.}

3.3 Elastic anisotropy

One important aspect that affects mechanical stability and structural strains of a material under various forms of stress is the elastic anisotropy. Anisotropy indices express the direction dependence mechanical characteristics of a system. Elastic anisotropy regulates a variety of physical processes, including the growth of plastic deformation in crystals, the propagation of microcracks in solids, the alignment/misalignment of quantum dots, phonon conductivity, and defect mobility. It also regulates the mechanical toughness of materials. Thus, an adequate understanding of anisotropic mechanical behavior is essential. Anisotropy and isotropy in crystals are typically dominated by covalent (directional) and metallic bonding, respectively [74, 75].

The degree of anisotropy in atomic bonding in various crystal planes can be determined by using the shear anisotropy factors. Three different factors given below can be used to measure the shear anisotropy in a hexagonal crystal [56, 76]:

$$A_1 = \frac{4C_{44}}{(C_{11} + C_{33} - 2C_{13})} \quad (11)$$

$$A_2 = \frac{4C_{55}}{(C_{22} + C_{33} - 2C_{23})} \quad (12)$$

$$A_3 = \frac{4C_{66}}{(C_{11} + C_{22} - 2C_{12})} \quad (13)$$

where A_1 , A_2 and A_3 are the respective shear anisotropy factors for {100}, {010}, {001} planes between <011> and <010> directions, <101> and <001> directions, and <110> and <010> directions, respectively.

Since $C_{11} = C_{22}$, $C_{44} = C_{55}$ and $C_{13} = C_{23}$ for hexagonal crystals, thus $A_1 = A_2$. When $A_1 = A_2 = A_3$, then the crystal is said to be isotropic with respect to shear, otherwise it is anisotropic. In Table 4, the estimated values of shear anisotropy of W_2N_3 are listed.

The following standard equations can be used to determine the universal anisotropy index (A^U), equivalent Zener anisotropy measure (A^{eq}), anisotropy in shear (A_G), and anisotropy in compressibility (A_B) of materials with any crystal symmetry.

$$A^U = 5 \frac{G_V}{G_R} + \frac{B_V}{B_R} - 6 \geq 0 \quad (14)$$

$$A^{eq} = \left(1 + \frac{5}{12}A^U\right) + \sqrt{\left(1 + \frac{5}{12}A^U\right)^2} \quad (15)$$

$$A^G = \frac{(G_V - G_R)}{2G^H} \quad (16)$$

$$A^B = \frac{(B_V - B_R)}{(B_V + B_R)} \quad (17)$$

One of the most used indices for measuring anisotropy in elastic characteristics is the universal anisotropy index (A^U). Regardless of the crystal symmetry, it is a single measure of anisotropy. Contrary to all other known anisotropy measures, A^U is the anisotropy parameter which takes account of both shear and bulk contributions. We may infer from Eqn. (14), that G_V/G_R has a stronger impact on the anisotropy index A^U than B_V/B_R . The value of A^U less than zero or larger than zero indicates variable degrees of anisotropy, whereas A^U is zero for an isotropic material. The estimated A^U of W_2N_3 is 19.82, which demonstrates highly anisotropic characteristics. For locally isotropic crystals, A^{eq} equals 1.0. At ambient pressure the estimated values of A^{eq} for W_2N_3 is 18.47, which also indicates that the crystal is highly anisotropic. A^G and A^B have values between 0 and 1. The ideal elastic isotropy and the maximum elastic anisotropy are represented, respectively, by $A^G = A^B = 0$ and $A^G = A^B = 1$. The values of A^G and A^B are respectively 0.62 and 0.65 which are listed in Table 4. These values imply that W_2N_3 has slightly larger anisotropy in compressibility than in shear.

The universal log-Euclidean anisotropy index is defined by a log-Euclidean formula as follows [77, 78]:

$$A^L = \sqrt{\left[\ln\left(\frac{B_V}{B_R}\right)\right]^2 + 5\left[\ln\left(\frac{C_{44}^V}{C_{44}^R}\right)\right]^2} \quad (18)$$

where C_{44}^V and C_{44}^R are, respectively, the estimated values of C_{44} from the Voigt and the Reuss limits. These values can be obtained as [77]:

$$C_{44}^V = \frac{5}{3} \frac{C_{44}(C_{11} - C_{12})}{3(C_{11} - C_{12}) + 4C_{44}} \quad (19)$$

and

$$C_{44}^R = C_{44}^V + \frac{3}{5} \frac{(C_{11} - C_{12} - 2C_{44})^2}{3(C_{11} - C_{12}) + 4C_{44}} \quad (20)$$

The expression for A^L is valid for every crystal symmetry, same as the universal anisotropy index. This index is true for all crystallographic point symmetry groups and is scaled appropriately for perfect isotropy. But when investigating extremely anisotropic crystallites, A^L is shown to be less sparse than A^U , making it more relevant for the present study. The absolute amount of anisotropy cannot be explained by A^U ; only the anisotropic nature. Hence, the difference between the averaged stiffness of C^V and C^R is used in A^L calculations, and it is thought to be more suitable for anisotropy studies. The range of A^L values is 0 to 10.26. Nearly 90% of solids have A^L values greater than 1. A^L is 0 in the event of perfect isotropy. The calculated value of A^L is 5.31, which is much greater than 1, suggesting high level of anisotropy. According to theory, higher (lower) A^L value indicates the presence of layered (non-layered) type structure [79-81]. In this study, the high value of A^L for W_2N_3 indicates strongly layered structure. Such layered feature can make a compound highly suitable for exfoliation and chemical intercalation.

Along a - and c -axis, the linear compressibility of a hexagonal crystal can be evaluated by using the following equations [82]:

$$\beta_a = \frac{(C_{33} - C_{13})}{D} \quad \text{and} \quad \beta_c = \frac{(C_{11} + C_{12} - 2C_{13})}{D} \quad (21)$$

with $D = (c_{11} + c_{12})c_{33} - 2(c_{13})^2$

The estimated values of β_a , β_c , and β_c/β_a are listed in Table 4. Crystals that are elastically isotropic have a unit value of β_c/β_a . The degree of elastic anisotropy in compression is quantified by the deviation of these factors from their unit value. Our estimated values imply once again that W_2N_3 is highly anisotropic.

Table 4. Shear anisotropy factor (A_1 , A_2 and A_3), the universal anisotropy index A^U , equivalent Zener anisotropy measure A^{eq} , anisotropy in shear A_G , anisotropy in compressibility A_B , universal log-Euclidean index A^L , linear compressibility (β_a and β_c) (TPa^{-1}), and their ratio β_c/β_a for W_2N_3 .

Phase	A_1	A_2	A_3	A^U	A^{eq}	A_G	A_B	A^L	layered	β_a	β_c	β_c/β_a
W_2N_3	0.085	0.085	1.0	19.83	18.47	0.62	0.65	5.31	Yes	0.0012	0.0281	23.5

With the help of the ELATE program [83], the directional dependencies of the Young's modulus (Y), linear compressibility (β), shear modulus (G), and Poisson's ratio (ν) of the W_2N_3 can be examined. Using the CASTEP code, the elastic stiffness matrices needed for

this investigation are computed. The isotropic nature of crystals is manifested in the uniform circular 2D and spherical 3D graphical representations. The degree of anisotropy increases with the deviations from these ideal shapes. Figs. 2 show the 3D view of Y , β , G , and ν for W_2N_3 together with the 2D projection on the xy -, zx -, and yz -planes. The minimum and maximum values of the parameters are shown by the curves in green and blue colors, respectively. From two dimensional representations, it is clear that all of the four parameters are anisotropic in zx - and yz -planes but are isotropic in the xy -plane. From 3D plots, it can be observed that the 3D figures of Y , β , G , and ν show a large departure from spherical form, indicating the degree of anisotropy. The anisotropy order is displayed graphically in 2D and 3D plots as $\nu > G > \beta > Y$. In addition, ELATE describes a quantitative analysis that lists the maximum and minimum values of Y , β , G , ν and their ratios, as listed in Table 5.

Table 5. The minimum limit, maximum limit and anisotropy of Young’s modulus (Y , in GPa), compressibility (β , in TPa^{-1}), shear modulus, (G , in GPa), and Poisson’s ratio (ν) of W_2N_3 .

Phase	Young’s modulus			Linear compressibility			Shear modulus			Poisson’s ratio		
	Y_{min}	Y_{max}	A_Y	β_{min}	β_{max}	A_β	G_{min}	G_{max}	A_G	ν_{min}	ν_{max}	A_ν
W_2N_3	32.78	456.78	13.93	1.09	25.33	23.23	11.84	165.57	13.98	0.0104	0.5804	56.03

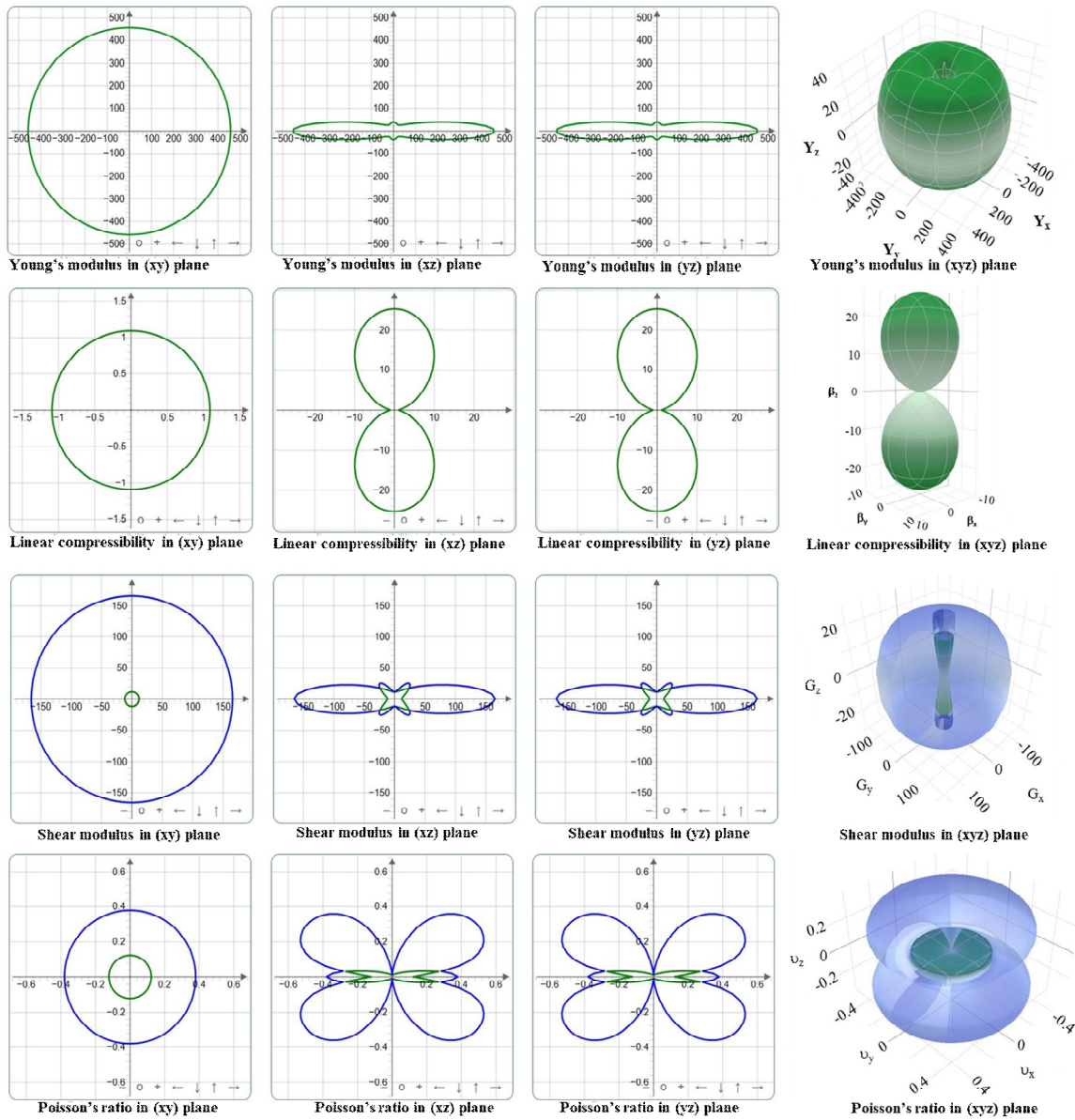


Fig. 2. Direction-dependence of Young's modulus (Y), compressibility (β), shear modulus (G), and Poisson's ratio (ν) of W_2N_3 single crystal.

3.4 Acoustic velocities and its anisotropy

A material's sound velocity is a significant characteristic that is correlated with its electrical and thermal conductivity. In recent years, physics, materials science, the design of musical instruments, seismology, geology, and the medical sciences have all taken notable interest in investigating the acoustic behavior of compounds and composites. Thermal conductivity is increased in a crystal structure with a higher sound velocity (v). The following equations [84-86] show how the bulk and shear moduli are related to the speed of transverse and longitudinal sound waves traveling through a crystalline material:

$$v_l = \left(\frac{3B + 4G}{3\rho} \right)^{1/2} \quad \text{And} \quad v_t = \left(\frac{G}{\rho} \right)^{1/2} \quad (22)$$

Using the following equation [84], the average sound velocity in a polycrystalline system is calculated from the transverse and longitudinal sound velocities:

$$v_m = \left[\frac{1}{3} \left(\frac{2}{v_t^3} + \frac{1}{v_l^3} \right) \right]^{-1/3} \quad (23)$$

In Table 6, the calculated acoustic velocities have been tabulated.

Each atom in a solid has three vibrational modes: one longitudinal and two transverse. Pure longitudinal and transverse modes only occur along certain axes in an anisotropic crystal. The propagating modes, on the other hand, are either quasi-transverse or quasi-longitudinal in all other directions. In W_2N_3 , pure transverse and longitudinal modes can only exist for the symmetry directions along [100] and [001] due to the hexagonal symmetry of the compound. The single crystal elastic constants can be used to calculate the acoustic velocities of W_2N_3 in these principal directions [87]:

[100] direction:

$$[100]_{vl} = \sqrt{\frac{(C_{11}-C_{12})}{2\rho}}; [010]_{vt1} = \sqrt{C_{11}/\rho}; [001]_{vt2} = \sqrt{C_{44}/\rho} \quad (24)$$

[001] direction:

$$[001]_{vl} = \sqrt{C_{33}/\rho}; [100]_{vt1} = [010]_{vt2} = \sqrt{(C_{44}/\rho)} \quad (25)$$

where v_l is the longitudinal sound velocity, ρ is the crystal density, and v_{t1} and v_{t2} are the first and second transverse acoustic modes, respectively. Table 7 lists the computed sound velocities for these directions. The longitudinal velocity of W_2N_3 along [100] is significantly higher than that along [001].

Table 6. Density ρ (g/cm^3), transverse sound velocity v_t (ms^{-1}), longitudinal sound velocity v_l (ms^{-1}), and average sound wave velocity v_m (ms^{-1}) of W_2N_3 .

Phase	ρ	v_t	v_l	v_m	Ref.
W_2N_3	14.28	2051.50	3592.35	2279.71	This work

Table 7. Anisotropic sound velocities (in ms^{-1}) in W_2N_3 along principal crystallographic directions.

Phase	Propagation directions	Sound velocity	
W_2N_3	[100]	$[100]_{vl}$	3404.87
		$[010]_{vt1}$	6121.44
		$[001]_{vt2}$	909.03
	[001]	$[100]_{vl}$	1648.36
		$[010]_{vt1}$	909.03
		$[001]_{vt2}$	909.03

3.5 Phonon dispersion – phonon DOS and phonon dynamics

The phonon dispersion spectra (PDS) and phonon density of states (PHDOS) can be employed to determine a variety of characteristics of a material. For example, about dynamical stability, phase transitions, and vibrational contributions of atoms to thermal expansion, heat capacity, and Helmholtz free energy from the phonon dispersion spectrum. The dynamical stability of a material is a crucial criterion for applications involving a time-varying applied loading. The phonon density of states and the electron-phonon interaction are intimately connected. The total phonon density of states in the ground state and the calculated phonon dispersion spectra of W_2N_3 in the high symmetry directions of the Brillouin zone (BZ) are shown in Fig. 3. If the phonon frequencies over the whole BZ are positive, a compound is expected to be dynamically stable. Soft phonon modes and dynamic instability are ensured to exist when negative phonon frequencies are present. Since W_2N_3 has 10 atoms per unit cell and the total number of phonon modes is three times the total number of atoms per unit cell, W_2N_3 contains 30 phonon modes. It has three acoustic modes colored by pink lines as shown in Fig. 3. There are 27 optical modes since a unit cell made up of N atoms has three acoustic modes and $(3N-3)$ optical modes. The coherent oscillations of atoms in a lattice outside of their equilibrium position are what give rise to acoustic phonons. In contrast, when one atom moves to the left and its neighbor moves to the right, the lattice's atoms oscillate out of phase, giving rise to the optical phonon. At Γ point, W_2N_3 exhibits the highest optical frequency and it is 20.80 THz.

The lattice dynamics of crystalline solids is particularly important for the zone-center phonon modes. Among the 27 optical modes, 12 are Raman active, 6 are IR active and the other 9 are

silent modes. The irreducible representations of the Brillouin zone-center optical phonon modes can be categorized in accordance with the factor group theory [88] as follows:

$$\Gamma_{opt.} = 2A_{2u} + 4E_{1u} + 6E_{2g} + 4E_{1g} + 2A_{1g} \quad (26)$$

where, A_{2u} and E_{1u} are IR active and E_{2g} , E_{1g} and A_{1g} are Raman active and B_{2g} , E_{2u} and B_{1u} are silent modes. When two or more modes have the same frequency yet cannot be distinguished from one another, they are referred to as degenerate modes. This is why there are six IR active modes and twelve Raman active modes included in Table 8. The highest frequencies observed in the IR and Raman active modes are 20.08 THz and 20.12 THz, respectively.

To see the contribution of each band to various atomic modes of vibration, we have also calculated the total and atomic partial PHDOS for W_2N_3 , which are displayed alongside the PDS. The PHDOS curve indicates that, whereas the higher optical branches (with frequencies > 15.7 THz) originate mainly from the vibration of lighter N-atoms, the acoustic and lower optical modes arise due to the vibration of heavier W atoms. Peaks in PHDOS are produced due to the flatness of the bands and the heights of the peaks in the total PHDOS are decreased due to the wide band dispersion. For W and N atoms, the prominent peaks in the PHDOS are seen around 5.27 THz and 20.10 THz, respectively.

Table 8. Theoretical wave-numbers ω_i and symmetry assignment of the IR-active and Raman-active modes of W_2N_3 .

Phase	Mode	Irr. Rep.	Wave-numbers, ω (cm ⁻¹)	
W_2N_3	IR	ω_1	A_{2u}	540.0
		ω_2	A_{2u}	669.3
		ω_3	E_{1u}	358.5
		ω_4	E_{1u}	476.1
	Raman	ω_1	E_{2g}	19.4
		ω_2	E_{2g}	351.2
		ω_3	E_{2g}	476.4
		ω_4	E_{1g}	80.3
		ω_5	E_{1g}	409.9
		ω_6	A_{1g}	180.3
		ω_7	A_{1g}	670.6

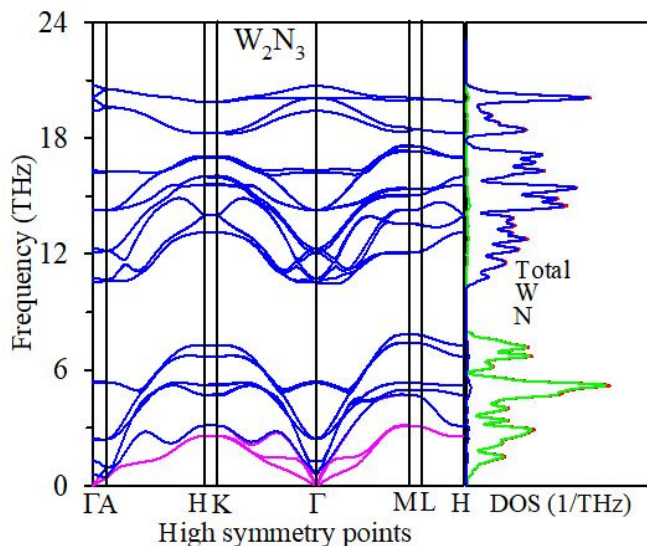


Fig. 3. The phonon dispersion spectra (PDS) and phonon density of states (PHDOS) of W_2N_3 .

3.6 Bonding character – charge density distribution

A useful tool for determining the type of interatomic chemical bonding is the electronic charge distribution map. It demonstrates how electrical charges around various atomic species are accumulated or depleted. Covalent bonding between two atoms is demonstrated by the accumulation of charges between them. A negative and positive charge balance at the atom locations is utilized to predict the presence of ionic bonds. On the other hand, uniform charge smearing shows metallic bonding. The electronic charge density in various crystal planes is shown in Fig. 4 in order to understand the chemical bonding between the atoms of W_2N_3 . The overall electron density is shown on the right-hand side of charge density maps using a color scale in the unit of $e/\text{\AA}^3$, with blue and red denoting high and low charge (electron) densities, respectively. Fig. 4 clearly shows that W atoms have comparatively high electron density than N atoms; covalent bonding exists between W and N atoms. Accumulation of charge also exists between W-W and N-N atoms. But, in the latter case the degree of covalency is comparatively weaker than that of W-N bonding. Hence, the compound possesses a mixture of covalent and metallic bonding.

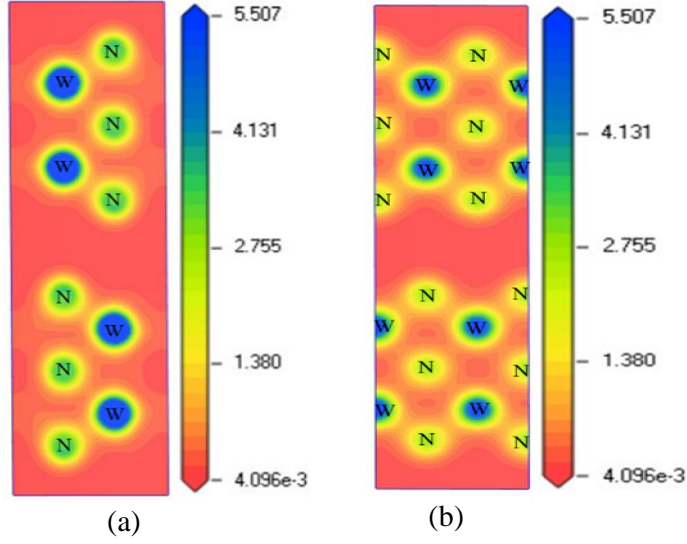


Fig. 4. Charge density distribution maps of W_2N_3 in (a) (111) and (b) (011) plane.

3.7 Thermophysical parameters

3.7.1. Debye temperature

The temperature at which the wavelength of phonons of a material nearly matches to the interatomic spacing is generally known as the Debye temperature Θ_D . It also defines a border line between the lattice vibration's classical and quantum characteristics. The high- and low-temperature behavior of a solid can be separated using this temperature. In order to comprehend several thermophysical features of solids, like melting temperature, bonding forces, thermal conductivity, the energy required for the creation of vacancies, specific heat, phonon dynamics, and superconductivity, it is crucial to study the Debye temperature. All vibrational modes have nearly the same energy, $k_B T$, when $T > \Theta_D$. However, it is found that at $T < \Theta_D$, the higher frequency modes are frozen. Debye temperature can be estimated using a variety of methods. When temperatures are low, only acoustic modes are responsible for the vibrational excitations. As a result, at low temperatures, the Debye temperature estimated from elastic constants agrees with that calculated from the specific heat measurement. In this study, the Debye temperature of W_2N_3 is calculated by Anderson technique, using the following equation [89]:

$$\Theta_D = \frac{h}{k_B} \left[\frac{3n}{4\pi V_0} \right]^{1/3} v_m \quad (27)$$

where n is the number of atoms within a unit cell, V_0 is the volume of a unit cell, k_B is Boltzmann's constant, h is Planck's constant, and v_m is mean sound velocity. Hexagonal W_2N_3 has a Debye temperature of ~ 380 K in the ground state which is enlisted in Table 9.

The Debye temperature of W_2N_3 is moderate which suggests that the atomic bonding strengths are not very strong and the material under study is not very hard in nature.

3.7.2 Phonon thermal conductivity

The transfer of heat through the vibrations of lattice ions within a solid is quantified by lattice (phonon) thermal conductivity. It is one of the most crucial thermal factors in determining the energy conversion efficiency of thermoelectric materials. Both phonons and electrons can carry thermal energy in solids. At low temperatures, electrons are the primary heat carriers in metals. The study of lattice thermal conductivity is essential for materials intended for high temperature applications. With a vast array of technical applications, including the development of novel thermoelectric materials, sensors, heat sinks, transducers, and thermal barrier coatings, the phonon thermal conductivity of solids, is one of the key thermophysical parameters. With a formula developed by Slack [90-92], the lattice thermal conductivity, k_{ph} as a function of temperature can be estimated as follows:

$$k_{ph} = A(\gamma) \frac{M_{av} \theta_D^3 \delta}{\gamma^2 n^{2/3} T} \quad (28)$$

where γ is the Grüneisen parameter, T is the absolute temperature, n is the total no. of atoms in the unit cell, M_{av} is the average atomic mass (in kg/mol) in a crystal, δ is the cubic root of the average atomic volume and θ_D is the Debye temperature $A(\gamma)$ is the γ dependent parameter that can be calculated from the following equation [93]:

$$A(\gamma) = \frac{4.85628 \times 10^7}{2 \left(1 - \frac{0.514}{\gamma} - \frac{0.228}{\gamma^2} \right)} \quad (29)$$

The room temperature (300 K) value of the calculated lattice thermal conductivity, k_{ph} , is enlisted in Table 9. Callaway–Debye theory [94] states that the lattice thermal conductivity at low temperatures is directly proportional to the Debye temperature, θ_D . The lattice thermal conductivity of a material increases with increasing θ_D . Furthermore, a material's lattice thermal conductivity and Young's modulus are correlated as: $K_{ph} \propto \sqrt{Y}$ [95]. The phonon thermal conductivity of W_2N_3 is high at room temperature (Table 9).

3.7.3 Grüneisen parameter

An important thermophysical parameter which estimates the anharmonic effects in a solid is known as the Grüneisen parameter γ . It is associated with several significant physical processes, including thermal conductivity, thermal expansion, acoustic wave absorption, and

the temperature dependence of elastic characteristics. The larger the value of γ , the higher is degree of anharmonicity. Using Poisson's ratio, the Grüneisen parameter of W_2N_3 can be estimated by using the following equation [96]:

$$\gamma = \frac{3(1+\nu)}{2(2-3\nu)} \quad (30)$$

The estimated value of W_2N_3 is 1.54, which is shown in Table 9. This value is typical for solids.

3.7.4 Melting temperature

A parameter of interest that restricts the temperature range in which a solid can be applied is the melting temperature (T_m). A solid will exhibit stronger atomic interaction, higher bonding energy, higher cohesive energy and lower coefficient of thermal expansion if it has high T_m [85, 97-99]. Solids can be continually utilized below T_m without chemical change or excessive distortion producing mechanical difficulties. With the use of elastic constants, the following empirical relationship can be used to determine a material's melting point [98]:

$$T_m = 345K + (4.5K/GPa) \left(\frac{2C_{11} + C_{33}}{3} \right) \quad (31)$$

The estimated melting temperature of W_2N_3 is 2008.5 K, which is listed in Table 9. Thus, W_2N_3 can be used as a promising candidate material for high temperature applications due to its high melting temperature. High heat of fusion, low fusion entropy, or a combination of both is the main causes of a high melting point.

3.7.5 Heat capacity

In addition to being necessary for many applications, the specific heat capacity offers crucial information into the material's vibrational characteristics. The constant volume heat capacity, C_v , goes to the Dulong-Petit limit at high temperatures and it is proportional to T^3 at very low temperature [99]. The specific heat capacity, at constant-volume, C_v , and at constant-pressure, C_p , for W_2N_3 with different temperatures at $P = 0$ GPa and different pressures at $T = 300$ K are respectively shown in Figs. 5 (a, b) and (c, d). The heat capacities of W_2N_3 increase as temperature rises due to phonon thermal softening, as seen in Fig. 5 (a, c). The specific heat capacities, C_v and C_p , exhibit a significant rise up to around 300 K as a result of the anharmonic approximation of the Debye model. As seen in Fig. 5 (c), at high temperature ($T > 300K$), the anharmonic impact on C_v is suppressed for W_2N_3 , and C_v approaches the

Dulong-Petit limit, which is typical for all solids. With the increase of pressure, C_v and C_p are seen to decrease as shown in Fig. 5 (b, d). The Debye temperature obtained within the quasi-harmonic approximation is ~ 399 K, quite close to the value estimated using the sound velocities.

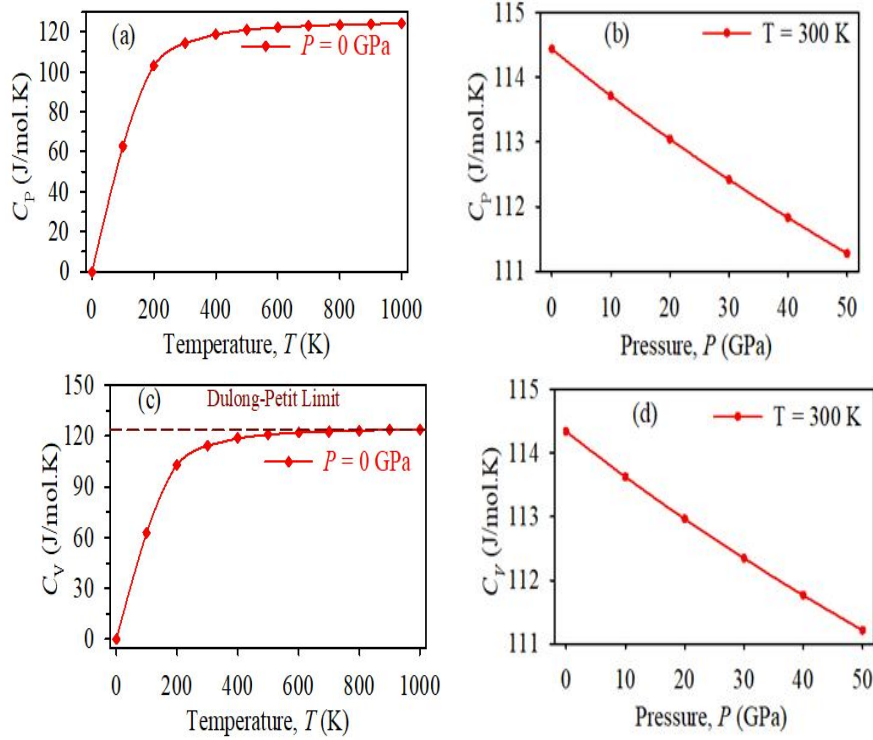


Fig. 5. Temperature and pressure dependent variations of specific heat capacities C_p and C_v of W_2N_3 .

3.7.6 Entropy

The entropy, S , is a broad aspect of a thermodynamic system that measures the amount of disordered energy content in a material. Figure 6 (a and b) demonstrate the change in entropy, S , as a function of temperature and pressure. With the rise of temperature, the entropy is seen to increase [Fig. 6(a)] as a consequence of increasing thermal disorder. Additionally, for $T = 300$ K, it is seen from Fig. 6(b) that the entropy falls with the increase of pressure. This is because when pressure increases, the volume of the solid drops.

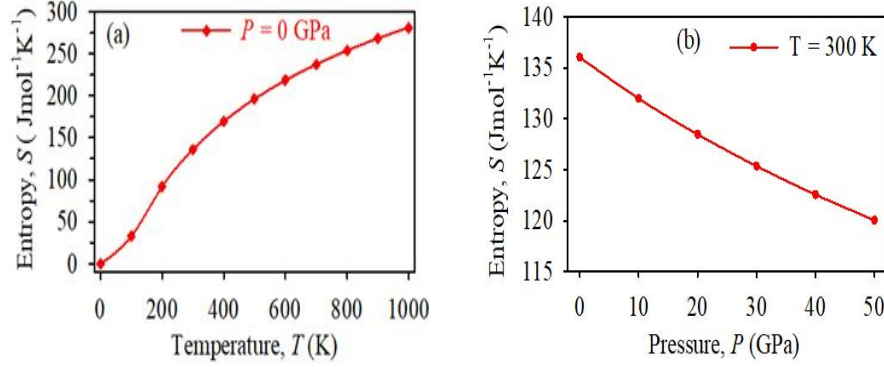


Fig. 6. Temperature and pressure dependent variations of entropy, S , of W_2N_3 .

Table. 9. Calculated melting temperature (T_m in K), Debye temperature (Θ_D in K), lattice thermal conductivity, k_{ph} (W/m-K) at 300 K, and Grüneisen parameter, γ for W_2N_3 .

Compound	T_m	Θ_D		k_{ph}	γ	Ref.
		Using elastic constant	Using QHD model			
W_2N_3	2008.5	380.2	399.3	16.5	1.54	This

3.8 Electronic properties

3.8.1 Band structure

In order to understand the electronic, optical, and magnetic characteristics of materials at the microscopic level, it is important to understand their electronic band structure. The effective masses of charge carriers can be calculated from band structure. It also greatly influences the charge transport and bonding properties. The nature of dominating bands close to the Fermi level can be used to better understand a material's charge transport characteristics. The electronic energy band structure of W_2N_3 has been calculated and is depicted in Fig. 7 along different high symmetry directions (Γ -A-H-K- Γ -M-L-H) in the momentum space. The horizontal broken line at zero energy indicates the Fermi level (E_F). The unit cell of W_2N_3 has 84 different energy bands in all. It is evident from Fig. 7 that there is no band gap at the Fermi level. This demonstrates the metallic character of hexagonal W_2N_3 in the optimized structure. The bands that cross the Fermi level are displayed in various colors along with the band numbers that correlate to each color. Mainly N-2p and W-5d states contribute to the energy bands near the Fermi level. This indicates that N-2p and W-5d states dominate the charge transport properties of W_2N_3 . It is noteworthy that the band crossing close to the Γ -point exhibits hole-like characteristic. All the bands crossing the Fermi level are found to be

fairly dispersive. We can better understand the underlying Fermi surfaces by using the band structure calculations.

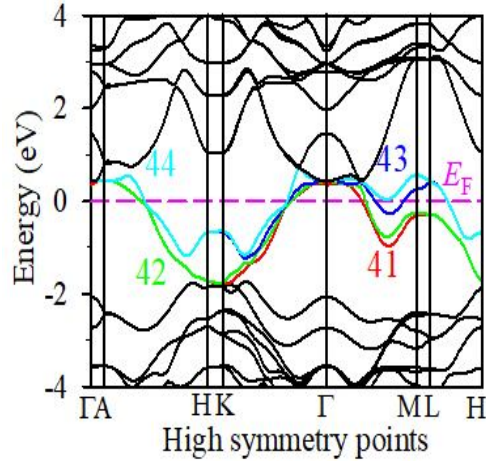


Fig. 7. Electronic band structure of W_2N_3 along several high symmetry directions in the Brillouin zone.

3.8.2 Density of states

The number of electronic states that are accessible to be occupied at each energy level per unit energy interval is referred to as the electronic energy density of states, or simply DOS. The structure of the DOS in the valence and conduction bands is connected to almost all of the electrical and optical characteristics of crystalline solids. The contribution of different atoms or orbitals to optoelectronic properties of a material can be understood by studying its total and partial density of states. The DOS of a material is also crucial to understand the contribution of each atom to bonding and antibonding states. Fig. 8 depicts the calculated total density of states (TDOS) and atom resolved partial density of states (PDOS) of W_2N_3 . The Fermi level, E_F , is shown by the vertical broken line at 0 eV. W_2N_3 exhibits metallic electrical conductivity, as indicated by the non-zero value of TDOS at the Fermi level E_F . It is found that W_2N_3 has a TDOS value of ~ 4.0 states per eV per unit cell or ~ 2.0 states per eV per formula unit at E_F . The highly dispersive bands crossing the Fermi level gives this low value of $N(E_F)$. In order to explain how W and N atoms contribute to TDOS and chemical bonding, the PDOS of these atoms has also been determined. In the vicinity of E_F , W $5d$ and N $2p$ dominantly contribute to the TDOS of W_2N_3 . Their respective values are 1.65 and 2.16 states per eV per unit cell at the Fermi level. The TDOS has large peaks at -3.77 and 2.88 eV that are close to the E_F . These bonding or anti-bonding peaks are the results of the

hybridizations of W $5d$ and N $2p$ electronic orbitals. Such hybridization close to the Fermi energy is frequently taken as an indication of the creation of strong covalent bonds.

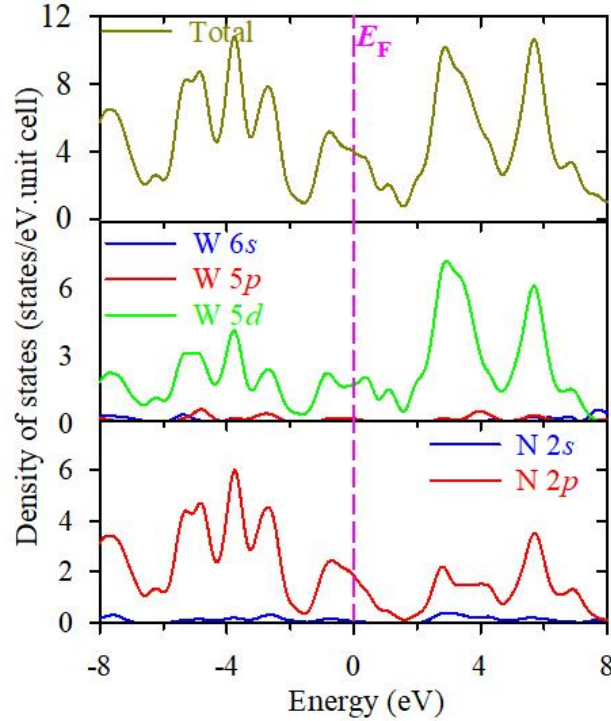


Fig. 8. Total and partial electronic density of states of W_2N_3 . The vertical line shows the Fermi energy.

3.8.3 Coulomb pseudopotential

The Coulomb pseudopotential is the measure of itinerant electron-electron interaction in a metal. It explains how coulomb repulsion affects superconductivity. The coulomb pseudopotential can be estimated by using the following equation [100]:

$$\mu^* = \frac{0.26N(E_F)}{1+N(E_F)} \quad (32)$$

The calculated value of the Coulomb pseudopotential is 0.173. This suggests that the electronic correlation in W_2N_3 is significant. This mainly arises due to significant contribution of the W $5d$ electrons to the TDOS at the Fermi level. The effective electron-phonon interaction that causes the Cooper pairs to develop in the context of superconductivity is reduced by the Coulomb pseudopotential. The superconducting transition temperature, T_c , decreases as a consequence [100-103].

3.8.4 Fermi surface

The Fermi surface (FS) topology controls the electronic properties of metals. The Fermi surface separates the occupied electronic states from the unoccupied electronic states at low temperature. The topology of a Fermi surface has a significant impact on a number of characteristics, including electronic, optical, thermal, and magnetic ones. The Fermi surface topology of W_2N_3 is shown in Fig. 9. (a, b, c and d). The 41, 42, 43 and 44 numbered bands cross the Fermi level (shown in Fig. 7), and are responsible for the construction of Fermi surface. The Fermi surface of W_2N_3 is made up of four Fermi sheets of different geometry. The FSs for the bands 41 and 42 are quite similar. Both the structures have circular-like sheets close to the center of the BZ. These are 2D electron-like sheets. On the other hand, the FSs for 43 and 44 bands are also similar and comparatively complex in shape. Here prismatic-like hexagonal cross sections are seen around the G - A direction. The remaining of these topologies consists of six separate parts parallel to the L - M directions. These are hole-like and located at the corner of the BZ. This implies that both electron- and hole-like behaviors exist in W_2N_3 . The Fermi surface topology also indicates that electronic transport is anisotropic in W_2N_3 . Close resemblance between the Fermi surfaces for bands 41 and 42, and bands 43 and 44 show that the pair of bands are highly degenerate.

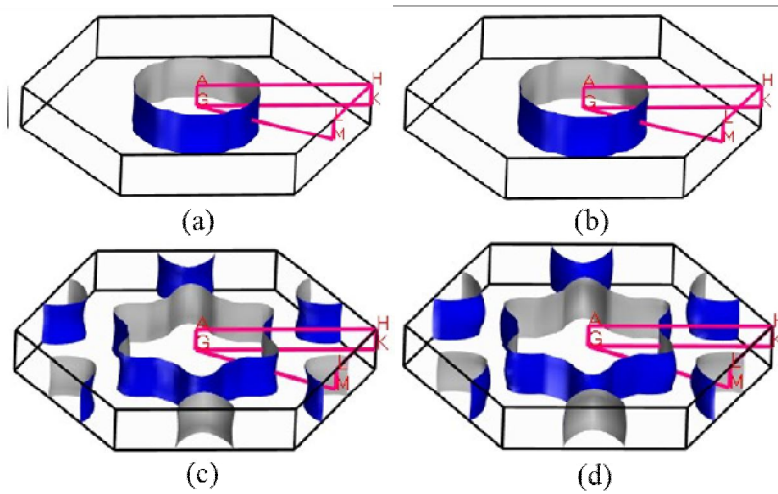


Fig. 9. Fermi surfaces of W_2N_3 for the band number (a) 41, (b) 42, (c) 43, and (d) 44.

3.9 Optical properties

The optical properties of a material indicate how it reacts to incident electromagnetic radiation. From the perspective of optoelectronic applications, the response to visible light is

crucial. In many areas of modern science and technology, including display devices, sensors, lasers, photo-electrodes, photo-detectors, photonics, solar cells, etc., the study of optical properties of solids has attracted significant interest. Additionally, optical anisotropy must be taken into account since various common optical technologies, such as 3D movie screens, LCD displays, polarizers, and wave plates, are developed using this [104]. Various energy/frequency dependent optical properties, notably the dielectric function, loss function, refractive index, optical conductivity, absorption coefficient, and reflectivity can completely determine the response of a material to incident light. We have estimated the optical properties of W_2N_3 for photon energies up to 30 eV for [100] and [001] polarization directions of the electric field as shown in Fig. 10 (a-h) to investigate the possible anisotropy. Electronic band structure and energy dependent density of states characteristics govern optical properties. For the investigation of optical properties, it is necessary to include Drude damping for metallic compound [105-108]. Since the band structure and density of states of W_2N_3 show that it is metal, a Drude damping of 0.05 eV and plasma frequency of 5 eV are used in order to calculate its optical properties.

The variations of the real and imaginary parts of the dielectric function, $\varepsilon(\omega)$, with respect to the photon energy, are respectively shown in Fig. 10 (a) and (b). In Fig. 10 (a), the real part, $\varepsilon_1(\omega)$, of the dielectric function vanishes at around 27 eV, which corresponds to a peak in the energy loss function as shown in Fig. 10 (h). The metallic conductivity of W_2N_3 is shown by the fact that $\varepsilon_1(\omega)$ goes through zero from below (negative value). It is also clear from Fig. 10 (b) that W_2N_3 is metallic in nature since the imaginary part of the dielectric function in both directions approaches to zero from above. Fig. 10 (b), also shows that the values of ε_2 drop to zero at 28 eV, suggesting that the material will become transparent above 28 eV energy.

A dimensionless quantity that characterizes how light travels through a medium is known as the refractive index. It is closely related to the local field inside the material as well as the electronic polarizability of ions. For designing photoelectric devices, the complex refractive index is a very significant factor. The phase velocity of the electromagnetic wave inside the sample is determined by the real part of the refractive index, whereas the extinction coefficient (imaginary part) spectrum reveals how much the incident electromagnetic radiation is attenuated while passing through the material. The frequency dependence of the refractive index of W_2N_3 for [100] and [001] polarization directions are respectively shown in

Figs. 10 (c) and (d). For both directions, refractive index of W_2N_3 is large at low energy and decreases with increasing energy. Due to high static refractive index value of W_2N_3 , it can be used in display devices.

The absorption coefficient (α) is the measure of the ability of a material to absorb incoming electromagnetic radiation. It is a useful measure for determining a material's electronic properties, regardless of whether it is metallic, semiconducting, or insulating [109]. The absorption coefficient plays a very important role to know how well a semiconducting material converts solar energy and how much light of specific energy can enter the material before being absorbed. The energy dependent absorption spectra of W_2N_3 for the polarization directions [100] and [001] are illustrated in Fig. 10 (e). In this figure, the nonzero value at zero photon energy is due to the metallic character of W_2N_3 , which is compatible with the dielectric function, DOS, and band structure calculations. For the [100] and [001] polarizations, the highest absorption is seen at about 9.6 eV and 19.1 eV, respectively. Significant optical anisotropy can be observed in the absorption properties in this way. From Fig. 10 (e), it is seen that, α decreases sharply at ~ 26.5 eV for both polarization directions, which agrees well with the position of loss peak as shown in Fig. 10 (h).

The conduction of free charge carriers over a certain range of photon energy can be characterized from the optical conductivity of a material. This is a dynamic response of mobile charge carriers, including the electron-hole pairs produced by photons in semiconductors. The real part of the photoconductivity (σ) spectra of W_2N_3 is shown in Fig. 10 (f). At zero photon energy, the nonzero photoconductivity for both directions manifests that, W_2N_3 has no electronic band gap, which agrees with previously calculated band structure and density of states. For W_2N_3 , the maximum photoconductivity is obtained at zero photon energy for both polarizations. W_2N_3 shows isotropic nature at low energy region and anisotropic nature after 1.26 eV. Generally, the low energy (infrared) portion of the spectra is dominated by the intraband contribution to the optical characteristics. The interband transition, on the other hand, causes peaks in the high energy region of the absorption and conductivity spectra. W_2N_3 exhibits the highest peaks in the visible and ultraviolet regions.

The reflectivity spectra of W_2N_3 along [100] and [001] polarizations as a function of incident photon energy is shown in Fig. 10 (g). The reflectivity of W_2N_3 exhibits significant optical anisotropy. From Fig. 10 (g), it is seen that, at ambient pressure the reflectivity of W_2N_3

begins from zero frequency with a value of 0.99. The reflectivity remains above 90% in the infrared region. Fig 10 (g) shows that W_2N_3 has lower reflectivity in the entire visible light regions in addition to the low-energy part of the UV region of the solar spectra. Nevertheless, W_2N_3 has above 44% reflectivity in the visible region and can be employed as a good solar heat reflector [107].

An important optical parameter that describes how much energy a fast moving electron loses when moving through a material is known as the loss function. In the dielectric formalism used to explain the optical spectra and the excitations created by fast charges in solids, the energy loss function of a material is a crucial quantity. A material's absorption, reflection and loss function properties are interconnected. The plasma resonance is connected with the peaks in the loss function spectrum, and the frequency that corresponds to those peaks is known as the plasma frequency (ω_p) [107]. The energy/frequency dependent electron energy loss function for W_2N_3 is depicted in Fig. 10 (h). It is interesting to note that the maxima of the loss function of W_2N_3 are found at 26.75 eV and 27.50 eV for [100] and [001] polarization directions, respectively. The sudden decrease in absorption coefficient and reflectivity of W_2N_3 as shown in Figs. 10 (e) and (g) can be linked to these sharp loss peaks. These frequencies (energies) are called bulk screened plasma frequency as the peak in loss function is associated with the plasma resonance. When $\epsilon_2 < 1$ and $\epsilon_1 = 0$, then the energy loss peak manifests in the high energy region [110, 111]. W_2N_3 will be transparent, and will switch from metallic to dielectric response if the incoming light frequency is greater than the plasma frequency.

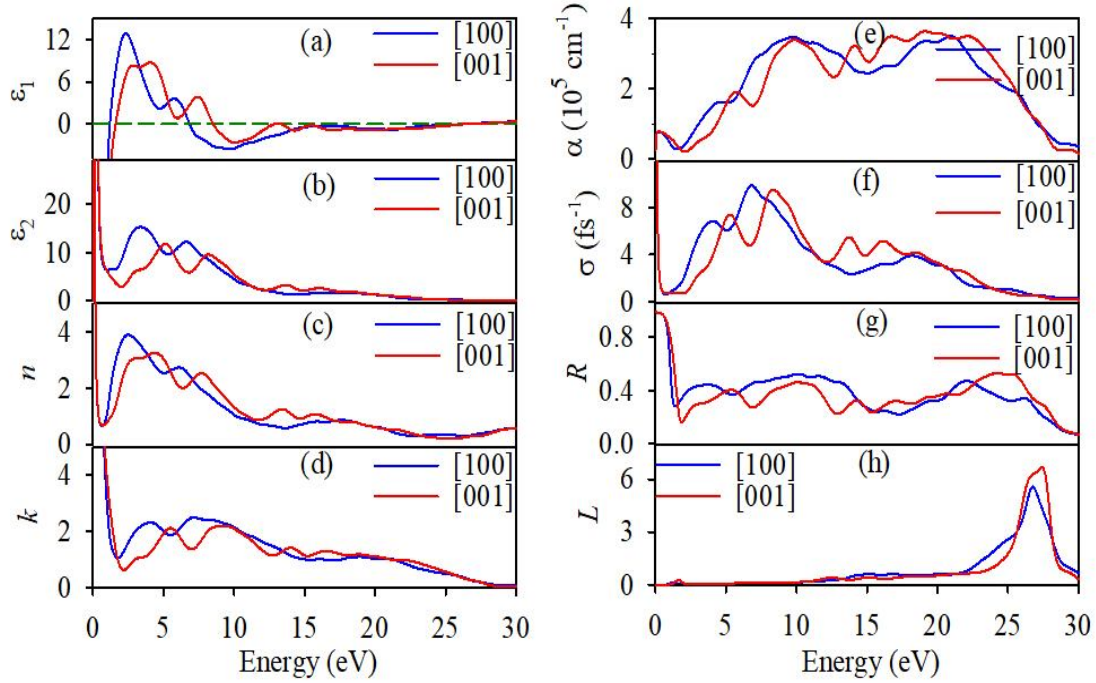


Fig. 10. Optical parameters of W_2N_3 as a function of photon energy.

3.10 Thermodynamic properties

The thermodynamic properties of W_2N_3 are evaluated in the temperature range of 0 to 1000 K and pressure range of 0 to 50 GPa pressure using quasi-harmonic approximation. The bulk modulus of a material is used to calculate its resistance to uniform compression. It also provides details on how well the material bonds together. Figs.11 (a) and 11 (b) reveal the temperature and pressure dependence of the isothermal bulk modulus of W_2N_3 . According to our findings, at temperatures below 150 K, the bulk modulus of W_2N_3 is almost flat; at temperatures over 150 K, it drops gradually as shown in Fig.11 (a). From Fig. 11 (b) it is seen that the bulk modulus of W_2N_3 increases with increasing pressure, which satisfies the general formula for bulk modulus, $B = v \frac{\Delta p}{\Delta v}$.

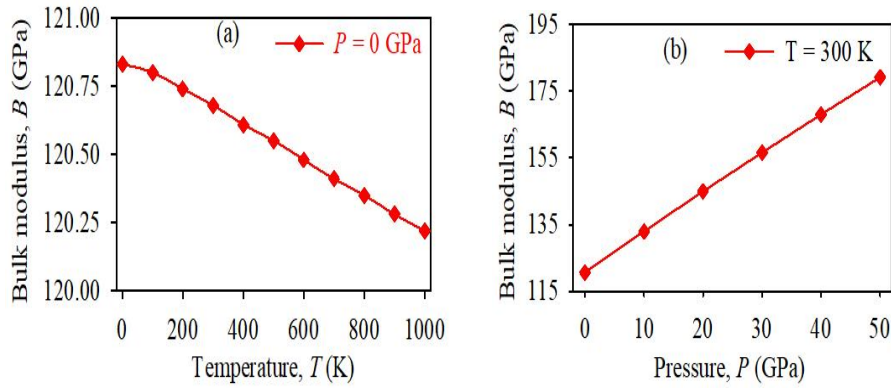


Fig. 11. Temperature and pressure dependent bulk modulus of W_2N_3 .

Figs. 12 (a) and (b) illustrate the volume thermal expansion coefficient (VTEC) with respect to temperature and pressure, respectively. Up to 300 K, the coefficients of W_2N_3 under investigation grow quickly; however, the increment is slow above 300 K. Conversely, as pressure is increased, the expansion coefficient falls but at different rates at a constant temperature of 300 K. It has been demonstrated that there is an inverse relationship between the bulk modulus and volume thermal expansion coefficient of a material.

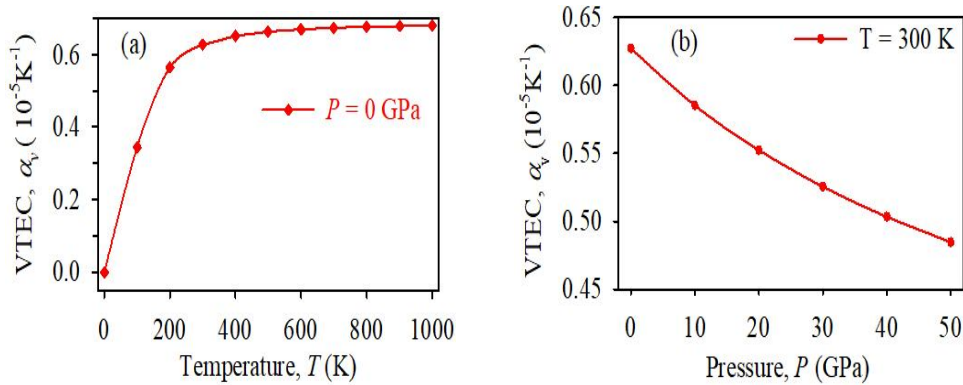


Fig. 12. Temperature and pressure dependent variations of volume thermal expansion coefficient of W_2N_3 .

The internal energy, denoted as U , is the energy content of a material due to all the activated degrees of freedom within. Figs. 13 (a and b), respectively, illustrates how the internal energy of W_2N_3 varies with temperature and pressure. The internal energy of W_2N_3 thus grows almost linearly with temperature above 100 K. Fig. 13(b) shows that the internal energy of W_2N_3 rises also almost linearly as pressure rises.

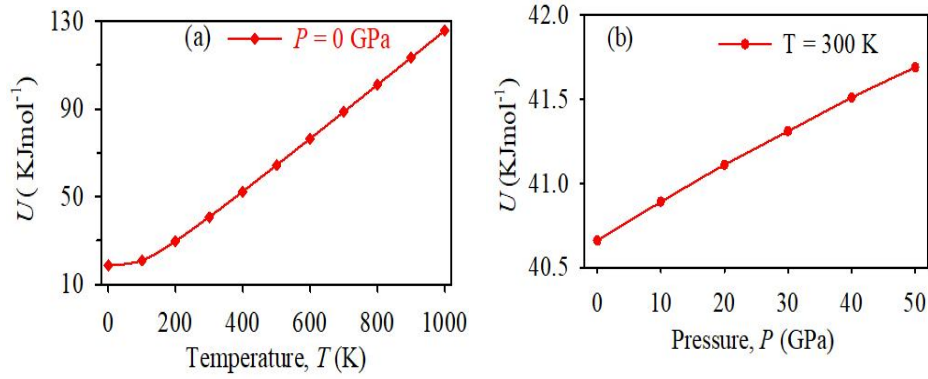


Fig. 13. Temperature and pressure dependent variations of internal energy of W_2N_3 .

4. Conclusions

The unexplored mechanical, vibrational, elastic, thermophysical, electronic, optical, and thermodynamic characteristics of W_2N_3 have all been investigated in this paper. Our investigation demonstrates the thermodynamical and mechanical stability of W_2N_3 . Phonon dispersion curves represent an illustration of the dynamical stability of our compound. W_2N_3 has a highly layered crystal structure, and is elastically anisotropic. W_2N_3 has borderline brittle characteristics, and its machinability level is extremely high. W_2N_3 has medium hardness. Combination of these features makes W_2N_3 an attractive compound for machine-tools device sector like some other engineering materials including the MAX and MAB phases [112-116]. The mechanical strength in W_2N_3 is controlled by both bond bending and bond stretching contributions. The charge density distribution of W_2N_3 shows direction dependence. There are significant covalent and metallic bondings. The substance being studied has a high melting point and a rather high phonon thermal conductivity at ambient temperature. Thus, it has potential to be used as a heat sink material. The electronic band structure shows metallic behavior with significant electronic correlations. The Fermi surface contains hole-like segments. The temperature and pressure dependent thermodynamic properties of W_2N_3 are conventional. The optical properties are anisotropic. The compound is an excellent infrared light reflector, and has a strong absorptivity of ultraviolet light. The reflectivity remains above 44% in the entire visible region, and it has high low-energy refractive index. These features make W_2N_3 suitable for optical device applications.

In conclusion, W_2N_3 has a number of appealing mechanical, thermal, and optoelectronic properties that make it a good fit for use in engineering and optical device applications. It is

our hope that the new findings in this work will encourage future theoretical and experimental investigations on W_2N_3 .

Acknowledgements

S. H. N. and R. S. I. acknowledge the research grant (1151/5/52/RU/Science-07/19-20) from the Faculty of Science, University of Rajshahi, Bangladesh, which partly supported this work. I. A. acknowledges the fellowship from the Ministry of Science and Technology, Bangladesh, for his M.Phil. research.

Data availability

The data sets generated and/or analyzed in this study are available from the corresponding author on reasonable request.

CRedit author statement

Istiak Ahmed: Methodology, Software, Formal analysis, Writing-Original draft. **F. Parvin:** Supervision, Writing-Reviewing and Editing. **R. S. Islam:** Writing-Reviewing and Editing. **S. H. Naqib:** Conceptualization, Supervision, Formal analysis, Writing- Reviewing and Editing.

Competing Interests

The authors declare no competing interests.

References

- 1 Sung CM, Sung M. Carbon nitride and other speculative super hard materials. *Mater Chem Phys* 1996;43:1. [https://doi.org/10.1016/0254-0584\(95\)01607-V](https://doi.org/10.1016/0254-0584(95)01607-V)
- 2 Haines J, Leger JM, Bocquillon G. Synthesis and Design of Superhard Materials. *Annu Rev Mater Res* 200;31:1. <https://doi.org/10.1146/annurev.matsci.31.1.1>
- 3 Zhao EJ, Meng JA, Ma YM, Wu Z. Phase stability and mechanical properties of tungsten borides from first principles calculations. *Phys Chem Chem Phys* 2010;12(40):13158. <https://doi.org/10.1039/c004122j>
- 4 Sun H, Jhi SH, Roundy D, Cohen ML, Loui SG. Structural forms of cubic BC_2N . *Phys Rev B* 2001;64(9):094108. <https://doi.org/10.1103/PhysRevB.64.094108>
- 5 Teter DM. Computational alchemy: the search for new super hard materials. *MRS Bull* 1998;23(1):22. <https://doi.org/10.1557/S0883769400031420>
- 6 Teter DM, Hemley RJ. Low-compressibility carbon nitrides. *Science* 1996;271:53. <https://www.jstor.org/stable/2890369>
- 7 Li Q, Wang M, Oganov AR, Cui T, Ma Y, Zou G. Rhombohedral super hard structure of BC_2N . *J Appl Phys* 2009;105:053514. <https://doi.org/10.1063/1.3086649>
- 8 Levine JB, Tolbert SH, Kaner RB. Advancements in the search for super hard ultra-incompressible metal borides. *Adv Funct Mater* 2009;19:3519. <https://doi.org/10.1002/adfm.200901257>

- 9 Levine JB, Nguyen SL, Rasool HI, Wright JA, Brown SE, Kaner RB. Preparation and properties of metallic, super hard rhenium diboride crystals. *J Am Chem Soc* 2008;130:16953. <https://doi.org/10.1021/ja804989q>
- 10 Zhao WJ, Wang YX. Elastic stability and electronic structure of low energy tetragonal and monoclinic PdN₂ and PtN. *Chin Phys B*. 2009;18:3934. <https://doi.org/10.1088/1674-1056/18/9/053>
- 11 Kroll, P, Schroter T, Peters M. Prediction of novel phases of tantalum (V) nitride and tungsten(VI) nitride that can be synthesized under high pressure and high temperature. *Angew Chem* 2005;44:4249. <https://doi.org/10.1002/anie.200462980>
- 12 Wang H, Li Q, Li Y, Xu Y, Cui T, Oganov AR, et al. Ultra-incompressible phases of tungsten dinitride predicted from first principles. *Phys Rev B* 2009;79:132109. <https://doi.org/10.1103/PhysRevB.79.132109>
- 13 Choi D, Kumta PN. Synthesis, Structure, and Electrochemical Characterization of Nanocrystalline Tantalum and Tungsten Nitrides. *J Am Ceram Soc* 2007;90:3113. <https://doi.org/10.1111/j.1551-2916.2007.01873.x>
- 14 Wriedt HA. The N-W (nitrogen-tungsten) system. *Bull Alloy Phase Diagrams* 1989;10:358. <https://doi.org/10.1007/bf02877592>
- 15 Schönberg N. Contributions to the Knowledge of the Molybdenum-Nitrogen and the Tungsten-Nitrogen Systems. *Acta Chem Scand*. 1954;8:204. <https://doi.org/10.3891/acta.chem.scand.08-0204>
- 16 Oyama ST. *The Chemistry of Transition Metal Carbides and Nitrides*. Blackie Academic & Professional: (Glasgow, 1996), Chapters 11-15. <https://doi.org/10.1007/978-94-009-1565-7>
- 17 Mc Milian PF. New materials from high-pressure experiments. *Nat Mater* 2002;1:19. <https://doi.org/10.1038/nmat716>
- 18 Zerr A, Miehe G, Riedel R. Synthesis of cubic zirconium and hafnium nitride having Th₃P₄ structure. *Nat Mater* 2003;2:185. <https://doi.org/10.1038/nmat836>
- 19 Headspith DA, Sullivan E, Greave C, Francesconi MG. Synthesis and characterisation of the quaternary nitride-fluoride Ce₂MnN₃F(2-δ). *Dalton Trans* 2009;42:9273. <https://doi.org/10.1039/b908591b>
- 20 Balasubramanian K, Khare S, Gall D. Vacancy-induced mechanical stabilization of cubic tungsten nitride. *Phys Rev B* 2016;94:174111. <https://doi.org/10.1103/PhysRevB.94.174111>
- 21 Liu ZTY, Zhou X, Gall D. First-principles investigation of the structural, mechanical and electronic properties of the NbO-structured 3d, 4d and 5d transition metal nitrides. *Comput Mater* 2014;84:365. <https://doi.org/10.1016/j.commatsci.2013.12.038>
- 22 Wang CC, Tao Q, Dong SS, Wang X, Zhu PW, et al. Synthesis and Mechanical Character of Hexagonal Phase δ-WN. *Inorg Chem* 2017;56:3970. <https://doi.org/10.1021/acs.inorgchem.6b03041>
- 23 Wang S, Yu X, Lin Z, Zhang RF, He DW, Qin JQ, et al. Synthesis, Crystal Structure, and Elastic Properties of Novel Tungsten Nitrides. *Chem Mater* 2012;24:3023. <https://doi.org/10.1021/cm301516w>
- 24 Zhao Z, Bao K, Duan D, Tian FB, Huang YP, Yu HY, et al. The low coordination number of nitrogen in hard tungsten nitrides: a first-principles study. *Phys Chem*

- Chem Phys 2015;17:13397. <https://doi.org/10.1039/c5cp00147a>
- 25 Pangilinan LE, Hu S, Akopov G, Cabrera SC, Yeung MT, Mohammadi R, et al. Superhard Materials: Advances in the Search and Synthesis of New materials. Inorganic Chemistry, John Wiley & Sons, Ltd. <https://doi.org/10.1002/9781119951438.eibc2076.pub2>
 - 26 Qin J, Zhang X, Xue Y. Structure and Mechanical Properties of Tungsten Mononitride under High Pressure from First-Principles Calculations. Comput Mater Sci 2013;79:456. <https://doi.org/10.1016/j.commatsci.2013.06.003>
 - 27 Ozsdolay BD, Mulligan, CP, Guerette M. Epitaxial Growth and Properties of Cubic WN on MgO(001), MgO(111), and Al₂O₃(0001). Thin Solid Films 2015;590:276. <https://doi.org/10.1016/j.tsf.2015.08.002>
 - 28 Lin Q, Sha L, Zhu C, Yao Y. New multifunctional tungsten nitride with energetic N₆ and extreme hardness predicted from first principles. Europhys Lett 2017;118:46001. <https://doi.org/10.1209/0295-5075/118/46001>
 - 29 Mounet N, Gibertini M, Schwaller P, Campi D, Merkys A, Marrazzo A, et. al. Two-dimensional materials from high-throughput computational exfoliation of experimentally known compounds. Nat Nanotechnol 2018;13:246. <https://dx.doi.org/10.1038/s41565-017-0035-5>
 - 30 Campi D, Kumari S, Marzari N. Prediction of phonon-mediated superconductivity with high critical temperature in the two-dimensional topological semimetal. Nano Letters 2021;21:3435. <https://doi.org/10.1021/acs.nanolett.0c05125>
 - 31 You JY, Gu B, Su G, Feng YP. Two-dimensional topological superconductivity candidate in a van der Waals layered material. Phys Rev B 2021;103:104503. <https://doi.org/10.1103/PhysRevB.103.104503>
 - 32 Kang Z, He HY, Ding R, Chen J, Pan BC. Structures of W_xN_y Crystals and Their Intrinsic Properties: First-Principles Calculations. Crystal Growth & Design 2018;18:2270. <https://doi.org/10.1021/acs.cgd.7b01707>
 - 33 Clark SJ, Segall MD, Pickard CJ, Hasnip PJ, Probert MIJ, Refson K, et al. First principles methods using CASTEP. Z Kristallogr 2005;220:567. <https://doi.org/10.1524/zkri.220.5.567.65075>
 - 34 Perdew JP, Burke K, Ernzerhof M. Generalized Gradient Approximation Made Simple. Phys Rev Lett 1996;77:3865. <https://doi.org/10.1103/physrevlett.77.3865>
 - 35 Vanderbilt D. Soft self-consistent pseudopotentials in a generalized eigenvalue formalism. Phys Rev B 1990;41:7892. <https://doi.org/10.1103/physrevb.41.7892>
 - 36 Monkhorst HJ, Pack JD. Special points for Brillouin-zone integrations. Phys Rev B 1976;13:5188. <https://doi.org/10.1103/PhysRevB.13.5188>
 - 37 Fischer TH, Almlof J. General methods for geometry and wave function optimization. J Phys Chem 1992;96:9768. <https://doi.org/10.1021/j100203a036>
 - 38 Murnaghan FD. Finite Deformation of an Elastic Solid, Wiley, (New York, 1951). <https://doi.org/10.1090/S0002-9904-1952-09627-0>
 - 39 Voigt W. Lehrbuch der Kristallphysik, (Taubner, Leipzig, 1928). <https://doi.org/10.1007/978-3-663-15884-4>
 - 40 Reuss A. Berechnung der Fließgrenze von Mischkristallen auf Grund der Plastizitätsbedingung für Einkristalle. Z Angew Math Mech 1929;9:49.

- <https://doi.org/10.1002/zamm.19290090104>
- 41 R. Hill. The Elastic Behaviour of a Crystalline Aggregate. Proc Phys Soc A 1952;65:349. <https://doi.org/10.1088/0370-1298/65/5/307>
 - 42 Kresse G, Furthmüller J, Hafner J. Ab initio force constant approach to phonon dispersion relations of diamond and graphite. Europhys Lett 1995;32:729. <https://doi.org/10.1209/0295-5075/32/9/005>
 - 43 Parlinski K, Li ZQ, Kawazoe Y. First-principles determination of the soft mode in cubic ZrO_2 . Phys Rev Lett 1997;78:4063. <https://doi.org/10.1103/PhysRevLett.78.4063>
 - 44 Naher MI, Naqib SH. Structural, elastic, electronic, bonding, and optical properties of topological CaSn_3 semimetal. J Alloys Compd 2020;829:154509. <https://doi.org/10.1016/j.jallcom.2020.154509>
 - 45 Blanco MA, Francisco E, Luana V, GIBBS: isothermal-isobaric thermodynamics of solids from energy curves using a quasi-harmonic Debye model. Comput Phys Commun 2004;158:57. <https://doi.org/10.1016/j.comphy.2003.12.001>
 - 46 Murnaghan FD. The Compressibility of Media under Extreme Pressures. Proc Natl Acad Sci USA 1944;30:244. <https://doi.org/10.1073/pnas.30.9.244>
 - 47 Birch F. Finite Elastic Strain of Cubic Crystals. Phys Rev 1947;71:809. <https://doi.org/10.1103/PhysRev.71.809>
 - 48 Wang Y, Zhao E, Zhao J, Fu L, Ying C, Lin L. Prediction of novel ground state and high pressure phases for W_2N_3 : First principles. Comput Mater Sci 2019;156:215. <https://doi.org/10.1016/j.commatsci.2018.09.054>
 - 49 Mouhat F, Coudert F. Necessary and sufficient elastic stability conditions in various crystal systems. Phys Rev B 2014;90:224104. <https://doi.org/10.1103/PhysRevB.90.224104>
 - 50 Kleinman L. Deformation Potentials in Silicon. I. Uniaxial Strain. Phys Rev 1962;128: 2614. <https://doi.org/10.1103/PhysRev.128.2614>
 - 51 Jamala M, Asadabadi SJ, Ahmad I. Elastic constants of cubic crystals. Comput Mater Sci 2014;95:592. <https://doi.org/10.1016/j.commatsci.2014.08.027>
 - 51 Gueddouh A, Bentria B, Lefkaier I. First-principle investigations of structure, elastic and bond hardness of Fe_xB ($x = 1, 2, 3$) under pressure. J Magn Magn Mater 2016;406:192. <https://doi.org/10.1016/j.jmmm.2016.01.013>
 - 53 Mattesini M, Ahuja R, Johansson B. Cubic Hf_3N_4 and Zr_3N_4 : a class of hard materials. Phys Rev B 2003;68:184108. <https://doi.org/10.1103/PhysRevB.68.184108>
 - 54 Majewski AJ, Vogl P. Simple model for structural properties and crystal stability of sp-bonded solids. Phys Rev B 1987;35:9666. <https://doi.org/10.1103/physrevb.35.9666>
 - 55 Clerc DG, Ledbetter HM. Mechanical hardness: a semi-empirical theory based on screened electrostatics and elastic shear. J Phys Chem Solids 1998;59:1071. [https://doi.org/10.1016/S0022-3697\(97\)00251-5](https://doi.org/10.1016/S0022-3697(97)00251-5)
 - 56 Ravindran P, Fast L, Korzhavyi P, Johansson B. Density functional theory for calculation of elastic properties of orthorhombic crystals: application to TiSi_2 . J App Phys 1998;84:4891. <https://doi.org/10.1063/1.368733>

- 57 Hadi MA, Kelaidis N, Naqib SH. Mechanical behaviors, lattice thermal conductivity and vibrational properties of a new MAX phase Lu₂SnC. *J Phys Chem Solid* 2019;129:162. <https://doi.org/10.1016/j.jpcs.2019.01.009>
- 58 Hossain MM, Ali MA, Uddin MM, Islam AKMA, Naqib SH. Origin of high hardness and optoelectronic and thermo-physical properties of boron-rich compounds B₆X (X = S, Se): a comprehensive study via DFT approach. *J App Phys* 2021;129:175109. <https://doi.org/10.1063/5.0047139>
- 59 Kim W, Strategies for engineering phonon transport in thermoelectrics. *J Mater Chem C* 2015;3:10336. <https://doi.org/10.1039/C5TC01670C>
- 60 Pettifor DG, Theoretical predictions of structure and related properties of intermetallics. *Mater Sci Technol* 1992;8:345. <https://doi.org/10.1179/mst.1992.8.4.345>
- 61 Pugh SF, XCII. Relations between the elastic moduli and the plastic properties of polycrystalline pure metals. *Philos Mag* 1954;45:823. <https://doi.org/10.1080/14786440808520496>
- 62 Frantsevich IN, Voronov FF, Bokuta SA. Elastic Constants and Elastic Moduli of Metals and Insulators Handbook. (Naukova Dumka Kiev 1983), p.60.
- 63 Mott PH, Dorgan JR, Roland CM. The bulk modulus and Poisson's ratio of incompressible materials. *J Sound Vib* 2008;312:572. <https://doi.org/10.1016/j.jsv.2008.01.026>
- 64 Fu H, Li D, Peng F, Gao T, Cheng X. Ab initio calculations of elastic constants and thermodynamic properties of NiAl under high pressures. *Comput Mater Sci* 2008; 44:774. <https://doi.org/10.1016/j.commatsci.2008.05.026>
- 65 Simunek A. How to estimate hardness of crystals on a pocket calculator. *Physical Review B* 2007;75:172108. <https://doi.org/10.1103/PhysRevB.75.172108>
- 66 Vitos L, Korzhavyi PA, Johansson B. Stainless steel optimization from quantum mechanical calculations. *Nature Mater* 2003;2:25. <https://doi.org/10.1038/nmat790>
- 67 Lincoln RC, Koliwad KM, Ghate PB. Morse-potential evaluation of second-and third-order elastic constants of some cubic metals. *Phys Rev* 1967;157:463. <https://doi.org/10.1103/PhysRev.162.854.2>
- 68 Puttlitz KJ, Stalter KA. Handbook of lead-free solder technology for microelectronic assemblies. (New York: Springer; 2005), p. 98. <https://doi.org/10.1201/9780203021484>
- 69 Phasha MJ, Ngoepe PE, Chauke HR. Link between structural and mechanical stability of fcc-and bcc-based ordered Mg–Li alloys. *Intermetallics* 2010;18:2083. <https://doi.org/10.1016/j.intermet.2010.06.015>
- 70 Sun Z, Music D, Ahuja R, Schneider JM. Theoretical investigation of the bonding and elastic properties of nanolayered ternary nitrides. *Phys Rev B* 2005;71:193402. <https://doi.org/10.1103/PhysRevB.71.193402>
- 71 Erdemir A. *Modern Tribology Handbook*, Vol. II, ed. B. Bhushan (CRC Press, Boca Raton, FL, 2001) p. 787. <https://doi.org/10.1201/9780849377877>
- 72 Holmberg K and Matthews A. in: *Coatings Tribology*. (Netherlands: Elsevier; 1994). p. 1.
- 73 Donnet C, Erdemir A. *Solid Lubricant Coatings: Recent Developments and Future*

- Trends. Tribology Letters 2004;17:389.
<https://doi.org/10.1023/b:tril.0000044487.32514.1d>
- 74 Connétable D. First-principles study of transition metal carbides. Mater Res Exp 2016;3:126502. <https://hal.science/hal-01578450>
- 75 Jong MD, Chen W, Angsten T, Jain A, Notestine R, Gamst A. Charting the complete elastic properties of inorganic crystalline compounds. Scientific Data 2015;2:150009. <https://doi.org/10.1038/sdata.2015.9>
- 76 Gao XP, Jiang YH, Zhou R, Feng J. Stability and elastic properties of Y-C binary compounds investigated by first principles calculations. J Alloys Compd 2014; 587:819. <https://doi.org/10.1016/j.jallcom.2013.11.005>
- 77 Kube CM, Jong MD. Elastic constants of polycrystals with generally anisotropic crystals. J Appl Phys 2016;120:165105. <https://doi.org/10.1063/1.4965867>
- 78 Arsigny V, Fillard P, Pennec X, Ayache N. Fast and simple calculus on tensors in the log euclidean framework. in Image Computing and Computer-Assisted Intervention, Lecture Notes in Computer Science, Eds. J. Duncan and G. Gerig (Springer-Verlag, 2005), Vol. 3749, pp. 115–122, ISBN 9783540293262. https://doi.org/10.1007/11566465_15
- 79 Nahar MI, Naqib SH. First-principles insights into the mechanical, optoelectronic, thermophysical, and lattice dynamical properties of binary topological semimetal BaGa₂. Results in Physics 2022;37:105507. <https://doi.org/10.1016/j.rinp.2022.105507>
- 80 Nahar MI, Naqib SH. An ab-initio study on structural, elastic, electronic, bonding, thermal, and optical properties of topological Weyl semimetal TaX (X = P, As). Scientific Reports 2021;11:5592. <https://doi.org/10.1038/s41598-021-85074-z>
- 81 Nahar MI, Naqib SH. A comprehensive study of the physical properties of Nb₂P₅ via ab initio technique. Results in Physics 2021;28:104623. <https://doi.org/10.48550/arXiv.2103.16027>
- 82 Milman V, Warren MC. Elasticity of hexagonal BeO. J Phys: Condens Matter 2001;13:5585. <https://doi.org/10.1088/0953-8984/13/2/302>
- 83 Gaillac R, Pullumbi P, Coudert F-X. ELATE: an open-source online application for analysis and visualization of elastic tensors. J Phys Condens Matter 2016;28(27): 275201. <https://doi.org/10.1088/0953-8984/28/27/275201>
- 84 Schreiber E, Anderson OL, Soga N, Elastic Constants and Their Measurements. (McGraw Hill, New York, 1973). <https://doi.org/10.1115/1.3423687>
- 85 Ahmed I, Parvin F, Islam AKMA, Kashem MA. Inverse-perovskites Sc₃GaX (X = B, C, N): A comprehensive theoretical investigation at ambient and elevated pressures. Comput Cond Matter 2023;35:e00808. <https://doi.org/10.1016/j.cocom.2023.e00808>
- 86 Ashby MF, Ferreira PJ, Schodek DL. Material Classes, Structure, and Properties. Nanomaterials, Nanotechnologies and Design, (2009), p.143
- 87 Sun L, Gao Y, Xiao B. Anisotropic elastic and thermal properties of titanium borides by first-principles calculations. J Alloys Compd 2013;579:457. <https://doi.org/10.1016/j.jallcom.2013.06.119>
- 88 Parlinski k, Li ZQ, Kawazoe Y. First-Principles Determination of the Soft Mode in Cubic ZeO₂. Phys Rev Lett 1997;78:4063.

- <https://doi.org/10.1103/PhysRevLett.78.4063>
- 89 Hadi MA, Roknuzzaman M, Chroneos. Naqib SH, Islam AKMA, Vovk RV. Elastic and thermodynamic properties of new $(Zr_{3-x}Ti_x)AlC_2$ MAX-phase solid solutions. *Comp Mat Sci* 2017;137:318. <https://doi.org/10.1016/j.commat.2017.06.007>
 - 90 Ali MA, Hossain MM, Uddin MM, Hossain MA, Islam AKMA, Naqib SH. Physical properties of new MAX phase borides M_2SB ($M = Zr, Hf$ and Nb) in comparison with conventional MAX phase carbides M_2SC ($M = Zr, Hf$ and Nb): Comprehensive insights. *J Mater Sci Technol* 2021;11:1000. <https://doi.org/10.1016/j.jmrt.2021.01.068>
 - 91 Morelli DT, Slack GA. High lattice thermal conductivity solids. In: Shinde SL, Goela JS, editors. *High Thermal Conductivity Materials*. (New York, NY: Springer; 2006). <https://lccn.loc.gov/2004049159>
 - 92 Dhakal C, Aryal S, Sakidja R, Ching WY. Approximate lattice thermal conductivity of MAX phases at high temperature. *J Eur Ceram Soc* 2015;35:3203. <https://doi.org/10.1016/j.jeurceramsoc.2015.04.013>
 - 93 Julian CL. Theory of heat conduction in rare-gas crystals. *Phys Rev* 1965;137: A128. <https://doi.org/10.1103/PhysRev.137.A128>
 - 94 Callaway J. Model for lattice thermal conductivity at low temperatures. *Phys Rev* 1959;113:1046. <https://doi.org/10.1103/PhysRev.113.1046>
 - 95 Kim W. Strategies for engineering phonon transport in thermoelectrics. *J Mater Chem C* 2015;3(40):10336. <https://doi.org/10.1039/C5TC01670C>
 - 96 Slack GA, The Thermal Conductivity of Nonmetallic Crystals. *Solid State Phys* 1979;34:1. [https://doi.org/10.1016/S0081-1947\(08\)60359-8](https://doi.org/10.1016/S0081-1947(08)60359-8)
 - 97 Fine ME, Brown LD, Marcus HL. Elastic constants versus melting temperature in metals. *Scr Metall* 1984;18:951. [https://doi.org/10.1016/0036-9748\(84\)90267-9](https://doi.org/10.1016/0036-9748(84)90267-9)
 - 98 Clarke DR. Materials selection guidelines for low thermal conductivity thermal barrier coatings. *Surf Coat Technol* 2003;163:67. [https://doi.org/10.1016/S0257-8972\(02\)00593-5](https://doi.org/10.1016/S0257-8972(02)00593-5)
 - 99 Petit AT, Dulong PL, Research on some important points of the theory of heat. *Ann Chem Phys* 1981;10:395.
 - 100 Bennemann KH, Garland JW, in *Superconductivity in d- and f- Band Metals*, edited by D. H. Douglas, AIP Conf. Proc. No. 4, Edited by Douglass DH. (AIP, New York, 1972), p.103. <https://lccn.loc.gov/74188879>
 - 101 Mridha MM, Naqib SH. Pressure dependent elastic, electronic, superconducting, and optical properties of ternary barium phosphides (BaM_2P_2 ; $M = Ni, Rh$): DFT based insights. *Physica Scripta* 2020;95:105809. <https://doi.org/10.48550/arXiv.2003.14146>
 - 102 Lin W, Xu JH, Freeman AJ. Electronic structure, cohesive properties, and phase stability of Ni_3V , Co_3V , and Fe_3V . *Phys Rev B* 1992;45:10863. <https://doi.org/10.1103/PhysRevB.45.10863>
 - 103 Christensen NE, Novikov DL. Calculated superconductive properties of Li and Na under pressure. *Phys Rev B* 2006;73:224508. <https://doi.org/10.1103/PhysRevB.73.224508>
 - 104 Naher MI, Naqib SH. Possible applications of Mo_2C in the orthorhombic and

- hexagonal phases explored via ab-initio investigations of elastic, bonding, optoelectronic and thermophysical properties. *Results Phys* 2022;37:105505. <https://doi.org/10.1016/j.rinp.2022.105505>
- 105 Murtaza G, Gupta SK, Seddik T, Khenata R, Alahmed ZA, Ahmed R. Structural, electronic, optical and thermodynamic properties of cubic $REGa_3$ (RE = Sc or Lu) compounds: Ab initio study. *J Alloys Compd* 2014;597:36. <https://doi.org/10.1016/j.jallcom.2014.01.203>
 - 106 Murtaza G, Sajid A, Rizwan M, Takagiwa Y, Khachai H, Jibrán M. First principles study of Mg_2X (X = Si, Ge, Sn, Pb): elastic, optoelectronic and thermoelectric properties. *Mater Sci Semicond* 2015;40:429. <https://doi.org/10.1016/j.mssp.2015.06.075>
 - 107 Reshak AH, Atuchin VV, Auluck S. First and second harmonic generation of the optical susceptibilities for the non-centro-symmetric orthorhombic $AgCd_2GaS_4$. *J Phys Condens Matter* 2008;20:325234. <https://doi.org/10.1088/0953-8984/20/32/325234>
 - 108 Li S, Ahuja R, Barsoum MW. Optical properties of Ti_3SiC_2 and Ti_4AlN_3 . *Appl Phys Lett* 2008;92:221907. <https://doi.org/10.1063/1.2938862>
 - 109 F. Yakuphanoglu, PhD thesis, Firat Universty (2002) (Unpublished).
 - 110 Saniz R, Ye LH, Shishidou T, Freeman AJ. Structural, electronic, and optical properties of $NiAl_3$: first-principles calculations. *Phys Rev B* 2006;74:14209. <https://doi.org/10.1103/PhysRevB.74.014209>
 - 111 Almeida de JS, Ahuja R. Electronic and optical properties of RuO_2 and IrO . *Phys Rev B* 2006;73:165102. <https://doi.org/10.1103/PhysRevB.73.165102>
 - 112 Hadi MA, Dahlqvist M, Christopoulos S-RG, Naqib SH, Chroneos A, Islam AKMA. Chemically stable new MAX phase V_2SnC : a damage and radiation tolerant TBC material. *RSC Adv* 2020;10:43783. <https://doi.org/10.1039/D0RA07730E>
 - 113 Hadi MA, Roknuzzaman M, Parvin F, Naqib SH, Islam AKMA, Aftabuzzaman M. New MAX phase superconductor Ti_2GeC : A first-principles study. *J Sci Res* 2014;6:11. <https://doi.org/10.3329/jsr.v6i1.16604>
 - 114 Hadi MA, Christopoulos S-RG, Chroneos A, Naqib SH, Islam AKMA. DFT insights into the electronic structure, mechanical behaviour, lattice dynamics and defect processes in the first Sc-based MAX phase Sc_2SnC . *Sci Rep* 2022;12:14037. <https://www.nature.com/articles/s41598-022-18336-z>
 - 115 Aktar MB, Parvin F, Islam AKMA, Naqib SH. Structural, elastic, electronic, bonding, thermo-mechanical and optical properties of predicted NbAlB MAB phase in comparison to MoAlB: DFT based ab-initio insights. *Results in Phys* 2023;52:106921. <https://doi.org/10.1016/j.rinp.2023.106921>
 - 116 Ali MA, Hadi MA, Hossain MM, Naqib SH, Islam AKMA. Theoretical investigation of structural, elastic, and electronic properties of ternary boride MoAlB. *Physica status solidi B* 2017;254:1700010. <https://doi.org/10.1002/pssb.201700010>